ISWFoam: A numerical model for internal solitary wave simulation in continuously stratified fluids

Jingyuan Li[1], Qinghe Zhang[1], Tongqing Chen[1]

[1]State Key Laboratory of Hydraulic Engineering Simulation and Safety, Tianjin University, Tianjin 300072, China

Correspondence to: Qinghe Zhang (qhzhang@tju.edu.cn)

Abstract. A numerical model, ISWFoam, for simulating internal solitary waves (ISWs) in continuously stratified, incompressible, viscous fluids is developed based on a fully three-dimensional (3D) Navier-Stokes equation using the open source code OpenFOAM. This model combines the density transport equation with the Reynolds-averaged Navier-Stokes equation with the Coriolis force, and the model discrete equation adopts the finite volume method. The *k-ω SST* turbulence model has also been modified accordingly to the variable density field. ISWFoam provides two initial wave generation methods to generate an ISW in continuously stratified fluids, including solving the weakly nonlinear models of the extended Korteweg–de Vries (eKdV) equation and the fully nonlinear models of the Dubreil-Jacotin-Long (DJL) equation. Grid independence tests for ISWFoam are performed, considering the accuracy and computing efficiency, the appropriate grid size of the ISW simulation is recommended to be one-one hundred and fiftieth of the characteristic length and one-twenty fifth of the ISW amplitude. Model verifications are conducted through comparisons between the simulated and experimental data for ISW propagation examples over a flat bottom section, including laboratory scale and actual ocean scale, a submerged triangular ridge, a Gaussian ridge and slope. The laboratory test results, including the ISW profile, wave breaking location, ISW arrival time, and the spatial and temporal changes in the mixture region, are well reproduced by ISWFoam. The ISWFoam model with unstructured grids and local mesh refinement can effectively simulate the evolution of ISWs, the ISW breaking phenomenon, waveform inversion of ISWs, and the interaction between ISWs and complex topography.

Key words. OpenFoam, Internal solitary wave tank, Stratified fluid, the DJL equation, Grid independence.

1. Introduction

Internal solitary waves (ISWs) are commonly observed in oceans, particularly on continental shelf

regions, due to strong tidal current flows over large topographic features (Huthnance, 1981), such as in the northern South China Sea (Alford et al., 2010; Alford et al., 2015; Cai et al., 2012). ISWs play an important role in both conveying nutrients from the deep ocean to shallower layers and promoting biological growth (Sandstrom et al., 1984). Additionally, ISWs are a potential threat to the ocean structures of resource exploration, exploitation, and submarine navigation vehicles (Alford et al., 2010; Osborne et al., 1980). A considerable number of studies, which include field measurements, remote sensing, experiments, theoretical analysis and numerical simulations, have been carried out due to the significance of ISWs (Vlasenko et al., 2005; Apel et al., 2006; Alford et al., 2011; Guo et al., 2014).

For numerically simulated ISWs, many models have been adopted, including the Euler equation, the inviscid/viscid incompressible Boussinesq model, the hydrostatic model, the non-hydrostatic model, and the VOF based two-phase flow model. Among these models, the representative hydrostatic models include the Naval Research Laboratory Ocean Nowcast/Forecast System (ONFS) (Ko et al.,2008), the Regional Hallberg Isopycnal Tide Mode (RHIMT) (Hallberg and Rhines, 1996; Hallberg, 1997), and the Ostrovsky-Hunter model. The representative non-hydrostatic models include the Bergen Ocean Model (BOM), the nonhydrostatic Regional Ocean Modeling System model (ROMS), the Stanford Unstructured Nonhydrostatic Terrain-following Adaptive Navier-Stokes Simulator (SUNTANS), and the Massachusetts Institute of Technology general circulation model (MITgcm). For example, Zhang et al (2012) established a variable water depth internal wave numerical model in a continuously stratified fluid system based on the Euler equation. Xu and Stastna (2020) used the viscid incompressible Boussinesq model to study cross-boundary-layer transport (Boegman and Stastna, 2019) by the fissioning process of shoaling ISWs. Lamb (1994) established a non-hydrostatic model, using a second-order projection method developed by Bell and Marcus (1992), which is used for internal wave research including boundary layer instability (Aghsaee et al., 2012), reflection (Lamb, 2009), and the interaction of the tides with the topography (Lamb, 2007; Aghsaee et al., 2010). Diamessis (2005) developed a spectral multidomain penalty method model and correctly reproduced the characteristic vorticity and internal wave structure. Subich et al (2013) developed a spectral collocation method for the solution of the Navier–Stokes equations under the Boussinesq approximation, and simulated the internal wave in continuously stratified fluid. Smedstad et al (2003) employed the ONFS model to establish a global ocean real-time forecasting system with an operational eddy resolution of 1/16°, which effectively tracks ocean

58 eddies, ocean currents and ocean fronts. Simmons et al (2004) employed the RHIMT model to carry out

59 a global numerical simulation of tidal currents, and analyzed the whole process of the conversion rate of

60 barotropic waves into baroclinic waves. Thiem (2011) used the Bergen Ocean Model to explore the

61 bottom boundary layer flow caused by waves beneath a propagating ISW in a two-fluid system. Li and

62 Farmer (2011) employed the Ostrovsky-Hunter model to study the nonlinear evolution of a

63 monochromatic internal wave. Buijsman et al (2010) employed ROMS model to study the asymmetry in

64 solitons to the east and west of Luzon Strait. Zhang et al (2011) used the nonhydrostatic SUNTANS

65 model (Fringer et al., 2006) to study the dynamics of A wave and B wave formation. Rayson et al (2018)

66 used the modified SUNTANS model to study the internal waves around Scott Reef and provided the

67 generation process of internal lee waves. Vlasenko et al (2010) employed the MITgcm model to

68 investigate the baroclinic tidal energy conversion in the area west of the Luzon Strait.

69   In summary, for continuously stratified fluids in complex ocean environments, numerical simulation

70 has become a leading method for ISW investigations. However, there are presently few versatile

71 numerical models with share code that can accurately simulate the ISW flow around complex topography

72 and submarine navigation vehicles in continuously stratified fluids. Therefore, the main objective of this

73 paper is to develop a solver, referred to as ISWFoam with a modified $k\text{-}\omega\ SST$ model that considers the

74 variable density field, which simulates the ISW in continuous density stratification, incompressible and

75 viscous fluids using the finite volume method with unstructured grids based on a fully three-dimensional

76 (3D) Navier-Stokes equation using the OpenFOAM library.

77   Notably, the open source field operation and manipulation code OpenFOAM®, as an object-

78 oriented C++ open source library that can be used to build a variety of solvers for computational fluid

79 problems based on the finite volume method, is becoming increasingly popular in the computational fluid

80 research community. At present, the official version of OpenFOAM® does not have a solver or boundary

81 conditions for solving the ISW in continuously stratified fluids. Although some researchers simulate

82 ISWs by modifying the OpenFOAM® code, most of these studies are based on a two-fluid system

83 without considering continuous stratification in density, such as Meng and Zhang (2016) and Li et al

84 (2017). Though recent work by Ding et al (2020) and Li et al (2021) considered continuous stratification

85 in density, their wave generation theories does not consider continuous stratification in density. To

86 extensively use of the numerical model of ISWs as a tool in the future, we will develop ISWFoam to

87   simulate the ISW in continuously stratified, incompressible and viscous fluids based on the OpenFOAM

88   library. The turbulence model will consider the variable density field. In addition, ISWFoam will provide

89   two initial methods to generate an ISW in continuously stratified fluids, including solving the weakly

90   nonlinear models of the extended Korteweg-de Vries (eKdV) equation and the fully nonlinear models of

91   the Dubreil-Jacotin-Long (DJL) equation. This approach renders the numerical model suitable for the

92   simulation of ISW flows in complex geometries and topographies. It is worth noting that ISWFoam does

93   not consider the generation process of ISWs, but focuses on the propagation and evolution of ISWs that

94   have already been generated, and the interaction between ISWs and complex structures and topography

95   on field scales.

96   The outline of the paper is described as follows. First, in Section 2, the governing equations for a

97   continuously stratified fluid are presented, and discrete forms of these equations are derived. Then, grid

98   independence tests of the developed ISWFoam model are described in Section 3. Subsequently, in

99   Section 4, a series of test cases are presented to verify the model. Simulation examples at the field scale

100   in Section 5. Finally, the conclusions are drawn in Section 6.

101   **2. ISWFoam: A three-dimensional numerical solver for ISWs in a continuously stratified fluid**

102   **2.1 Governing equations**

103   We present an ISW numerical model by solving the motion of a three-dimensional, viscous,

104   incompressible fluid with the Boussinesq approximation and rigid lid hypothesis. The governing

105   equations of the model are

106     $$\nabla \cdot \mathbf{U} = 0, \tag{1}$$

107     $$\frac{\partial \mathbf{U}}{\partial t} + \left(\mathbf{U} \cdot \nabla \right) \mathbf{U} - \nabla \cdot \left(v_{Eff} \nabla \mathbf{U} \right) = \mathbf{Q} \quad \mathbf{Q} = \frac{1}{\rho_0} \left(-\nabla p_{\_rgh} - \mathbf{g} \cdot \mathbf{X} \nabla \rho - \Omega e_3 \right), \tag{2}$$

108     $$\frac{\partial \rho}{\partial t} + \left(\mathbf{U} \cdot \nabla \right) \rho = \nabla \cdot \left(k \nabla \rho \right), \tag{3}$$

109   where $\mathbf{U} = (u_i, u_j, u_k)$ is the velocity vector, t is time, ∇ is the gradient operator, $\mathbf{Q}$ is the source term, ρ_0

110   is the reference density, ρ is the density field, $p_{\_rgh}$ is a modified pressure field, $\mathbf{g}$ is the gravitational

111   acceleration vector, and $\mathbf{X}$ is the position vector. v_{Eff} is the effective kinematic viscosity defined as $v_{Eff} =$

112   μ_{Eff}/ρ_0, where μ_{Eff} is the effective dynamic viscosity including the molecular viscosity (μ_l) and turbulent

113   viscosity (μ_t). k is the diffusion coefficient, and its value is the same as the effective dynamic

114 viscosity(μ_{Eff}). Ω is the Coriolis parameter, which is the twice the speed of rotation around the vertical

115 unit vector $e_3 = (0, 0, 1)$. ISWFoam uses a modified pressure $p_{\_rgh}$ instead of a total pressure p, and their

116 relationship is given by

117
$$p_{\_rgh} = p - \rho \mathbf{g} \cdot \mathbf{X}, \ \nabla p_{\_rgh} = \nabla p - \rho \mathbf{g} - \mathbf{g} \cdot \mathbf{X} \nabla \rho, \tag{4}$$

118 The upper boundary ($z = H$, with H the depth of computation domain) is treated as a rigid lid, the

119 kinematic boundary conditions for this boundary are given by

120
$$u_k(x, y, H, t) = 0 \tag{5}$$

121 To close the above equations, the turbulence model needs to be employed. The two-equation k-ε

122 model is widely used as an effective turbulence model, but it cannot capture the proper behaviour of

123 turbulent boundary layers up to separation due to adverse pressure gradients (Wilcox, 1993). For the

124 above boundary layers separation problem, Bardina et al. (1997) and Menter et al. (2003) suggested the

125 use of the k-ω Shear Stress Transport (SST) model to obtain substantially more accurate results. Therefore,

126 the turbulence model used in this paper is the k-ω SST model. Notably that in OpenFOAM, the

127 incompressible version for turbulence models does not consider the variable density field, and instead, it

128 treats the density as a constant, such as the k-ω SST model

129
$$\frac{\partial k}{\partial t} + \nabla \cdot (\mathbf{U}k) = \nabla \cdot \left[\left(\nu_{Eff} + \sigma_k \nu_t \right) \nabla k \right] + P_k^* - \beta^* \omega k \tag{6}$$

130
$$\frac{\partial \omega}{\partial t} + \nabla \cdot (\mathbf{U}\omega) = \nabla \cdot \left[\left(\nu_{Eff} + \sigma_\omega \nu_t \right) \nabla \omega \right] + C_\gamma \frac{\omega}{k} P_k - C_\beta \omega^2 + 2(1 - F_1) \frac{\sigma_{\omega 2}}{\omega} \nabla k \cdot \nabla \omega \tag{7}$$

131
$$P_k^* = \min(P_k, c_1 C_\mu k \omega) \tag{8}$$

132
$$\nu_t = \frac{a_1 k}{\max \left(a_1 \omega, \sqrt{2} S_t F_2 \right)} \tag{9}$$

133 where k is the turbulent kinetic energy, ω is the specific dissipation rate, P_k is the production term of k,

134 $P_k = \tau^R : \nabla \mathbf{U}$, P_k^* is related to the production term of turbulence kinetic energy P_k in the k equation, ν_t

135 is the turbulent kinematic viscosity, S_t is the mean rate of the flow strain, $S_t = 0.5(\nabla \mathbf{U} + \nabla \mathbf{U}^T)$, the model

136 constants are assigned the values $\beta^* = 0.09$, $a_1 = 0.31$, $c_1 = 10$ and $C_\mu = 0.09$, F_1 and F_2 are blending

137 functions, the value of σ_k, σ_ω, C_γ and C_β are blended using the equation $\Phi = F_1 \Phi_1 + (1 - F_1) \Phi_2$ in which

138 Φ_1 and Φ_2 are given in Table 1.

139

Table 1 Default values for Φ_1 and Φ_2

Φ	σ_k	σ_ω	C_β	C_γ
Φ_1	0.85	0.5	0.075	5/9

Φ_2	1.0	0.856	0.0828	0.44

Considering the variable density field during the solution process, it is necessary to consider the change in the density field in the turbulence model. Therefore, we modify the turbulence model to consider the change in density, and finally a modified *k-ω SST* model that considers the change in density is used to close the equation

$$\frac{\partial \rho k}{\partial t} + \nabla \cdot (\rho \mathbf{U} k) = \nabla \cdot \left[\rho \left(v_{Eff} + \sigma_k v_t \right) \nabla k \right] + \rho P_k^* - \rho \beta^* \omega k \tag{10}$$

$$\frac{\partial \rho \omega}{\partial t} + \nabla \cdot (\rho \mathbf{U} \omega) = \nabla \cdot \left[\rho \left(v_{Eff} + \sigma_\omega v_t \right) \nabla \omega \right] + C_\gamma \frac{\omega}{k} P_k - C_\beta \rho \omega^2 + 2(1-F_1) \rho \frac{\sigma_{\omega 2}}{\omega} \nabla k \cdot \nabla \omega \tag{11}$$

2.2 Numerical discretization

The governing equations are numerically discretized using the finite volume method based on the C++ open source library of OpenFOAM. The finite volume method requires that Eqs. (2) and (3) are satisfied over the control volume V_P around point P in integral form:

$$\int_{V_P} \int_{\Delta t} \left[\frac{\partial \mathbf{U}}{\partial t} + (\mathbf{U} \cdot \nabla) \mathbf{U} - \nabla \cdot (v_{Eff} \nabla \mathbf{U}) \right] dV dt = \int_{V_P} \int_{\Delta t} \mathbf{Q} \, dV dt, \tag{12}$$

$$\int_{V_P} \int_{\Delta t} \left[\frac{\partial \rho}{\partial t} + (\mathbf{U} \cdot \nabla) \rho - \nabla \cdot (k \nabla \rho) \right] dV dt = 0, \tag{13}$$

where Δt is the time step.

The momentum equation in ISWFoam is solved by constructing a predicted velocity field and then using the Pressure Implicit with Splitting of Operators (PISO) algorithm (Issa, 1986) to modify it. *n* is defined to represent the current moment. The PISO iteration process is marked as *m*; when *m* is equal to zero, it represents the current time (t^n).

First, only the temporal, convection and diffusion terms appear in the discrete version of the equation momentum, and the other terms are ignored. After this operation, we obtain an explicit expression for the predicted velocity field $\mathbf{U}_P^r$, namely,

$$\frac{\mathbf{U}_P^r - \mathbf{U}_P^n}{\Delta t} V_P + \sum_{f \in \partial V_P} \left(\phi_f^n \mathbf{U}_f^r \right) - \sum_{f \in \partial V_P} v_{Eff} \nabla \mathbf{U}_f^r \cdot \mathbf{S}_f = 0, \tag{14}$$

where *P* represents the centre of the grid cell, $\phi_f^n = \mathbf{U}_f^n \cdot \mathbf{S}_f$ is the volume flux at the initial time *n* and

164    $\mathbf{S}_f$ is the face vector.

165   The solution process requires the velocity on the surface f. Assuming the variation in $\mathbf{U}_f^r$ between

166   the centre P of the grid and the centre N of the adjacent grid, the face values are calculated using a mixture

167   method (blended differencing) of the central scheme (central differencing) and the upwind scheme

168   (upwind differencing) as follows (Jasak, 1996):

169    $$\mathbf{U}_f = \left(1-\lambda_U\right)\left(\mathbf{U}_f\right)_{UD} + \lambda_U\left(\mathbf{U}_f\right)_{CD} \tag{15}$$

170   where

171    $$\left(\mathbf{U}_f\right)_{UD} = \begin{cases} \mathbf{U}_P \text{ for } \phi_f \geq 0, \\ \mathbf{U}_N \text{ for } \phi_f < 0, \end{cases} \text{ and } \left(\mathbf{U}_f\right)_{CD} = \frac{\mathbf{U}_P + \mathbf{U}_N}{2} \tag{16}$$

172   where N represents the centre of the adjacent grid cells, $\phi_f = \mathbf{U}_f \cdot \mathbf{S}_f$ is volume flux. The limiter λ_U

173   can be selected from several alternatives (OpenFOAM, 2019), including linear, QUICK, vanLeer, etc. In

174   the following derivation process, the vanLeer scheme was used to calculate the velocity of the face centre

175    $$\mathbf{U}_f = \frac{1}{2}\left(\mathbf{U}_P + \mathbf{U}_N\right) + \frac{1}{2}\left[\psi(\phi_f)(1-\lambda_U)\right]\left(\mathbf{U}_P - \mathbf{U}_N\right), \tag{17}$$

176   where $\psi(\phi_f)$ is a step function defined by

177    $$\psi(\phi_f) = \begin{cases} 1 \text{ for } \phi_f \geq 0, \\ -1 \text{ for } \phi_f < 0, \end{cases} \tag{18}$$

178   Inserting Eq. (17) into Eq. (14) yields

179    $$A_P\mathbf{U}_P^r = \sum_{f \in \partial V_P} A_N\mathbf{U}_P^m + \frac{\mathbf{U}_P^n}{\Delta t} = H(\mathbf{U}^m) \tag{19}$$

180   After some manipulation, the quantities A_P and A_N are given as

181    $$A_P = \left\{\frac{V_P}{\Delta t} + \sum_{f \in \partial V_P} \frac{\phi_f^n}{2}\left[1 + \psi(\phi_f)(1-\lambda_U)\right] + \sum_{f \in \partial V_P} \nu_{Eff,f}\frac{|\mathbf{S}_f|}{|d|}\right\}\frac{1}{V_P} \tag{20}$$

182    $$A_N = \left\{-\frac{\phi_f^n}{2}\left[1 - \psi(\phi_f)(1-\lambda_U)\right] + \nu_{Eff,f}\frac{|\mathbf{S}_f|}{|d|}\right\}\frac{1}{V_P} \tag{21}$$

183   Including the effect of gravity and the Coriolis force in Eq. (19)

184    $$\mathbf{U}_P^r = \frac{H(\mathbf{U}^m)}{A_P} - \frac{\left(\mathbf{g}\cdot X\nabla\rho/\rho_0\right)^n}{A_P} - \frac{\left(\Omega e_3\right)^n}{A_P}, \tag{22}$$

185 Notably, that when m is equal to zero, it represents the initial moment n, and the value of the initial

186 moment is known. Therefore, we obtain the predicted velocity field $\mathbf{U}_P^r$ in the first iteration. We define

187 the surface gradient operator ($\nabla_{\frac{1}{f}}$), and the type of gradient operator acting on $\mathbf{U}$ is

188 $\nabla_{\frac{1}{f}} \mathbf{U} = \left(\mathbf{U}_N^m - \mathbf{U}_P^m\right)\big/|d|$, which represents the distance from the centre of the grid N to P. Similarly,

189 the surface gradient operator ($\nabla_{\frac{1}{f}}$) acting on scalar γ is $\nabla_{\frac{1}{f}} \lambda = \left(\lambda_N^m - \lambda_P^m\right)\big/|d|$. The associated flux

190 ($\phi_f = \mathbf{U}_f \cdot \mathbf{S}_f$) is achieved by executing an inner product with a surface vector ($\mathbf{S}_f$) on the left and right

191 parts of Eq. (22), giving

$$\phi_f^r = \left(\frac{H(\mathbf{U}^m)}{A_P}\right)_f \cdot \mathbf{S}_f - \left(\left(\frac{1}{A_P}\right)_f (\mathbf{g}\cdot\mathbf{X})_f^n \left(\frac{1}{\rho_0}\nabla_{\frac{1}{f}}\rho\right)^n |\mathbf{S}_f|\right) - \left(\frac{(\Omega e_3)^n}{A_P}\right)_f \cdot \mathbf{S}_f, \tag{23}$$

193 Eq. (23) completed the flux calculation without considering the influence of the pressure term. The

194 pressure contribution in terms of a flux can be expressed as

$$\left(\frac{-\nabla p_{\_rgh}}{\rho_0 A_P}\right)_f \cdot \mathbf{S}_f = \left(\frac{-1}{A_P}\right)_f \left(\frac{1}{\rho_0}\nabla_{\frac{1}{f}} p_{\_rgh}^{m+1}\right)|\mathbf{S}_f|, \tag{24}$$

196 Then, Eq. (24) is now added to Eq. (23) to yield

$$\phi_f^{m+1} = \left(\frac{H(\mathbf{U}^m)}{A_P}\right)_f \cdot \mathbf{S}_f - \left(\left(\frac{1}{A_P}\right)_f (\mathbf{g}\cdot\mathbf{X})_f^n \left(\frac{1}{\rho_0}\nabla_{\frac{1}{f}}\rho\right)^n |\mathbf{S}_f|\right) - \left(\frac{(\Omega e_3)^n}{A_P}\right)_f \cdot \mathbf{S}_f - \left(\frac{1}{A_P}\right)_f \left(\frac{1}{\rho_0}\nabla_{\frac{1}{f}} p_{\_rgh}^{m+1}\right)|\mathbf{S}_f| \tag{25}$$

198 Combined with Eq. (23), Eq. (25) is simplified and rewritten as

$$\phi_f^{m+1} = \phi_f^r - \left(\frac{1}{A_P}\right)_f \left(\frac{1}{\rho_0}\nabla_{\frac{1}{f}} p_{\_rgh}^{m+1}\right)|\mathbf{S}_f| \tag{26}$$

200 Using conservation of mass, we solve the pressure field $p_{\_rgh}^{m+1}$, which results in

$$\sum_{f \in \partial V_P}\left(\frac{1}{A_P}\right)_f \left(\frac{1}{\rho_0}\nabla_{\frac{1}{f}} p_{\_rgh}^{m+1}\right)|\mathbf{S}_f| = \sum_{f \in \partial V_P} \phi_f^r \tag{27}$$

202 The preconditioned conjugate gradient method is used to solve the linear system constructed by Eq.

203 (27) (OpenFOAM, 2019). After $p_{\_rgh}^{m+1}$ is obtained using Eq. (27), we calculate the volume flux using

204 Eq. (26) for each face. The cell centred velocity fields $\mathbf{U}_P^{m+1}$ are calculated by reconstructing the face

205 velocity flux using the following expression (Deshpande, 2012)

$$\mathbf{U}_P^{m+1} = \mathbf{U}_P^r + \left(\frac{1}{A_P}\right)\left(\sum_{f \in \partial V_P} \frac{\mathbf{S}_f \mathbf{S}_f}{|\mathbf{S}_f|}\right)^{-1} \cdot \left(\sum_{f \in \partial V_P} \left(\frac{\phi_f^{m+1} - (\mathbf{U}_P^r)_f \cdot \mathbf{S}_f}{(1/A_P)_f}\right)\frac{\mathbf{S}_f}{|\mathbf{S}_f|}\right) \tag{28}$$

206

Eq. (28) completes the velocity field calculation of the first iteration step in the PISO algorithm. By

converting the identifier m to $m+1$, the next PISO iteration is completed and updating the velocity in Eq.

(19) with the velocity $\mathbf{U}_P^{m+1}$ calculated from Eq. (28), thereby updating $p_{\_rgh}$, ϕ_f and $\mathbf{U}$. This procedure

is performed M times to guarantee that the results of the velocity and pressure together conform to the

continuity and momentum equations. Considering that PISO iteration levels require more than 1, but

typically not more than 4 (OpenFOAM, 2019), we specify that the number of PISO iteration levels is 3

in the computations presented in this paper. After completing the three iterations, the converged values

are considered the result of the next time step ($n + 1$), namely,

$$\phi_f^{n+1} = \phi_f^M, \quad \mathbf{U}_P^{n+1} = \mathbf{U}_P^M, \quad p_{\_rgh}^{n+1} = p_{\_rgh}^M, \tag{29}$$

We discretize the convection-diffusion equation of density (Eq. (13)) to obtain

$$\frac{V_P}{\Delta t}(\rho_P^{n+1} - \rho_P^n) + \sum(\phi_f^{n+1}\rho_f^{n+1}) = \sum k\left[|\mathbf{S}_f|\frac{\rho_N^{n+1} - \rho_P^{n+1}}{|d|}\right], \tag{30}$$

At the end of the iteration procedure, we bring the results of the volume flux into Eq. (30) to

calculate the density field at the next time (ρ_P^{n+1}), thereby updating the density field for the next step

calculation ($\Delta t = t^{n+2} - t^{n+1}$).

2.3 Initialized field of ISW generation

ISW generation methods mainly include the gravity collapse mechanism, double push-pedals

method (Fu et al., 2008), velocity-inlet method (Gao et al., 2012), mass source method (Wang et al.,

2018), initialization method, and methods addressing the interaction between tidal current and

topography. For example, Hsieh et al (2014) investigated the flow evolution of a depression ISW

generated by the gravity collapse mechanism. Cheng et al (2020) studied the interaction between ISWs

and a cylinder using the gravity collapse mechanism. The initialization method involves solving the

internal solitary wave theory at the initial moment, such as the Korteweg-de Vries (KdV) equation

(Grimshaw et al., 2010), the modified KdV (mKdV) equation, the extended KdV (eKdV) equation, the

forced KdV equation, the Ostrovsky equation (Li and Farmer, 2011), the Miyata-Choi-Camassa (MCC)

model (Miyata 1985 and 1988; Choi and Camassa, 1999), and the Dubreil-Jacotin-Long (DJL) equation

232 (Long, 1953; Turkington, 1991; Brown and Christie, 1997; Dunphy et al., 2011), to obtain the wave

233 surface, velocity field. The method of an interacting between tidal current and terrain that stimulates

234 ISWs is adopted by many scholars, such as Farmer and Smith (1980), Lamb et al (1994), and Shaw et al

235 (2009).

236   In this paper, the method of initializing the field is selected to generate the ISWs. To increase the

237 application range of the ISWFoam model, two initialization methods are provided, including solving the

238 weakly nonlinear models of the eKdV equation (Helfrich and Melville, 2006) and the fully nonlinear

239 models of the DJL equation for continuously stratified fluids (Turkington, 1991; Dunphy et al, 2011).

240 The Dubreil-Jacotin-Long (DJL) equation is expressed as

241
$$\nabla^2 \eta + \frac{N^2(z-\eta)}{c^2}\eta = 0, \quad \eta = 0 \quad \text{at} \quad z = 0, -H$$
$$\eta = 0 \quad \text{at} \quad |x| \to \infty$$
(31)

242 where η is the isopycnal displacement, H is the water depth, c is the propagation speed, N is the definition

243 of the buoyancy frequency, and z is vertical position.

244
$$N^2(z) = -g\frac{d\rho_0(z)}{dz},$$
(32)

245 where $\rho_0(z)$ is the reference density, and g is the gravitational acceleration.

246   By solving the above DJL equation we can obtain η and c, and then through the relationship $\psi = \eta c$,

247 where ψ is the stream function, we can obtain the wave-induced velocity field. We use the DJLES open

248 source package provided by Dunphy et al (2011) to solve the DJL equations. Then we input the initial

249 field calculated by DJLES into OpenFOAM to obtain the initial field required for OpenFOAM numerical

250 simulation.

251   Another theory of ISWFoam model wave generation involves the weakly nonlinear models of the

252 eKdV equation. Using the first order stream function for the DJL equation, we can obtain the well-known

253 KdV equation and further obtain the eKdV equation. For the specific derivation, please refer to the paper

254 by Lamb and Yan (1996). The eKdV equation (Helfrich and Melville, 2006) is

255
$$\frac{\partial \zeta}{\partial t} + (c_0 + c_1\zeta + c_3\zeta^2)\frac{\partial \zeta}{\partial x} + c_2\frac{\partial^3 \zeta}{\partial x^3} = 0,$$
(33)

256
$$c_0^2 = \frac{gh_1h_2(\rho_2 - \rho_1)}{\rho_1h_2 + \rho_2h_1},$$
(34)

$$c_1 = -\frac{3c_0}{2} \frac{\rho_1 h_2^2 - \rho_2 h_1^2}{\rho_1 h_1 h_2^2 + \rho_2 h_1^2 h_2}, \tag{35}$$

$$c_2 = \frac{c_0}{6} \frac{\rho_1 h_1^2 h_2 + \rho_2 h_1 h_2^2}{\rho_1 h_2 + \rho_2 h_1}, \tag{36}$$

$$c_3 = \frac{3c_0}{h_1^2 h_2^2} \left[\frac{7}{8} \left(\frac{\rho_1 h_2^2 - \rho_2 h_1^2}{\rho_1 h_2 + \rho_2 h_1} \right)^2 - \frac{\rho_1 h_2^3 + \rho_2 h_1^3}{\rho_1 h_2 + \rho_2 h_1} \right], \tag{37}$$

where ζ is the isopycnal vertical displacement; c_0 is the linear phase speed; the coefficients c_1, c_2 and c_3 are functions of the steady background stratification and shear through the linear eigenmode (vertical structure function) of interest (Helfrich and Melville, 2006); h_1 and h_2 are the mean upper and lower layer depths, respectively; ρ_1 and ρ_1 are the fluid densities of the upper and lower layers, respectively. The theoretical solution of Eq. (33) above is

$$\zeta = \frac{a}{B + (1 - B) \cosh^2 \left[\lambda_{eKdV} (x - c_{eKdV} t) \right]}, \tag{38}$$

$$\lambda_{eKdV}^2 = \frac{a}{12 c_2} \left(c_1 + \frac{1}{2} c_3 a \right), \tag{39}$$

$$c_{eKdV} = c_0 + \frac{a}{3} \left(c_1 + \frac{1}{2} c_3 a \right), \tag{40}$$

$$B = \frac{-a c_3}{2 c_1 + a c_3}, \tag{41}$$

$$u_1 = -c_{eKdV} \frac{\zeta}{h_1 - \zeta}, \ u_2 = c_{eKdV} \frac{\zeta}{h_2 + \zeta}, \tag{42}$$

where a is the ISW amplitude, λ_{eKdV} is the wavelength, c_{eKdV} is the wave speed, B is an auxiliary parameter, and u_1 and u_2 are the speeds of the upper and lower layers of the fluid, respectively. The waveform and velocity field of the ISWs are solved at the initial moment by the developed function and then assigned to the calculation domain.

The vertical profile of the initial density is given by a hyperbolic tangent function profile (Aghsaee et al., 2010)

$$\overline{\rho}(z) = \frac{\rho_1 + \rho_2}{2} - \frac{\rho_2 - \rho_1}{2} \tanh \left(\frac{z - z_{pyc}}{d_{pyc}} \right) \tag{43}$$

where z is the vertical position; ρ_1 and ρ_2 are the fluid densities of the upper and lower layers, respectively; z_{pyc} is the location of the centre of the pycnocline; and d_{pyc} is the thickness of the pycnocline. In this paper, unless otherwise specified, the form of the density profile adopts Eq. (43). The internal solitary wave

280 surface is obtained by calculating the gradient of the density field, and the absolute value of the maximum

281 value of the gradient represents the vertical position of the wave surface. Notably, the density profile of

282 the actual ocean is not always hyperbolic, so our model provides a function for users to modify the

283 density profile according to the actual situation.

284 **2.3.1 Comparison between the DJL equation and the eKdV equation**

285 To compare the DJL equation and the eKdV equation, we set up a numerical simulation, which

286 includes a tank that is 15 m long, 1 m wide and has a water depth of 0.5 m. The depths of the upper (h_1)

287 and lower (h_2) layers are 0.1 m and 0.4 m, respectively, the densities of the upper and lower layers are

288 1022 kg/m^3 and 1028 kg/m^3, respectively, the location of the centre of the pycnocline (z_{pyc}) is 0.4 m, the

289 pycnocline thickness (d_{pyc}) is 0.04 m vertically, the initial ISW amplitude (a) is 0.065 m and the location

290 of the centre of ISW is 12.5m. The ISWs propagate from right to left. The measuring point P is set at a

291 position 10m away from the initial ISW. The grid is uniform in the x-direction, y-direction and z-direction,

292 and the sizes are $\Delta x = 1 \times 10^{-2}$ m, $\Delta y = 1 \times 10^{-2}$ m and $\Delta z = 1 \times 10^{-3}$ m, respectively. Slip boundary conditions

293 are applied to the bottom and both sides, while cyclic boundary conditions are assigned to the inlet and

294 outlet boundaries. The top boundary is a rigid lid. The boundary conditions related to the density field

295 are no-flux boundary conditions.

296 Fig. 1 shows the comparison of the horizontal velocity component field when the DJL equation and

297 the eKdV equation are used to generate ISWs. At the initial moment, the ISW generated by the eKdV

298 equation is not as smooth as the ISW generated by the DJL equation, and the horizontal velocity at the

299 interface area is discontinuous as shown in Fig. 1(a) and (b). With the propagation of ISWs, the ISWs

300 generated by the DJL equation are always smooth at the interface area, and the velocity field is always

301 continuous as shown in Fig. 1(a), (c), (e) and (g). Correspondingly, the ISW generated by the eKdV

302 equation gradually produces a gradient in the vertical direction of the horizontal velocity in the interface

303 area, thus, the interface area becomes smooth, and the velocity becomes continuous. Fig. 1(d) shows this

304 evolution process, which is basically completed in 5s as shown in Fig. 1(f). At 50s, the difference between

305 the horizontal velocity fields of the two equations is very small as shown in Fig. 1(g) and (h).
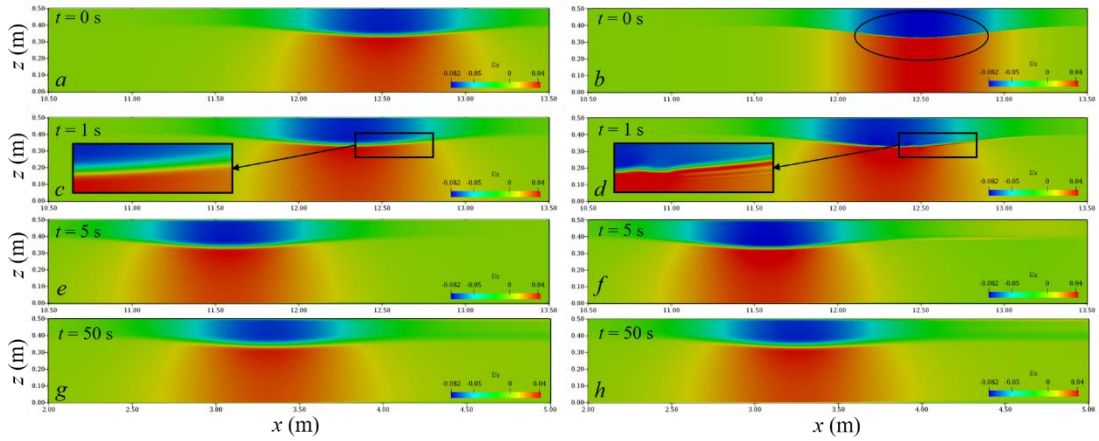
Figure 1: Comparison chart of the horizontal velocity component field: DJL equation (left) and eKdV equation (right).

Fig. 2 shows the comparison of the vertical velocity component field when the DJL equation and the eKdV equation are used to generate ISWs. Since the theoretical solution of the eKdV equation only obtain the average horizontal velocity of the upper and lower layers of the fluid, there is no vertical velocity at the initial moment, as shown in Fig. 2(b). With the propagation of ISWs, the vertical velocity field will gradually be generated and finally stabilized, and the stable time occurs at 5s as shown in Fig. 2(b), (d), (f) and (h). At 50s, the difference between the vertical velocity fields of the two equations is very small as shown in Fig. 2(g) and (h).
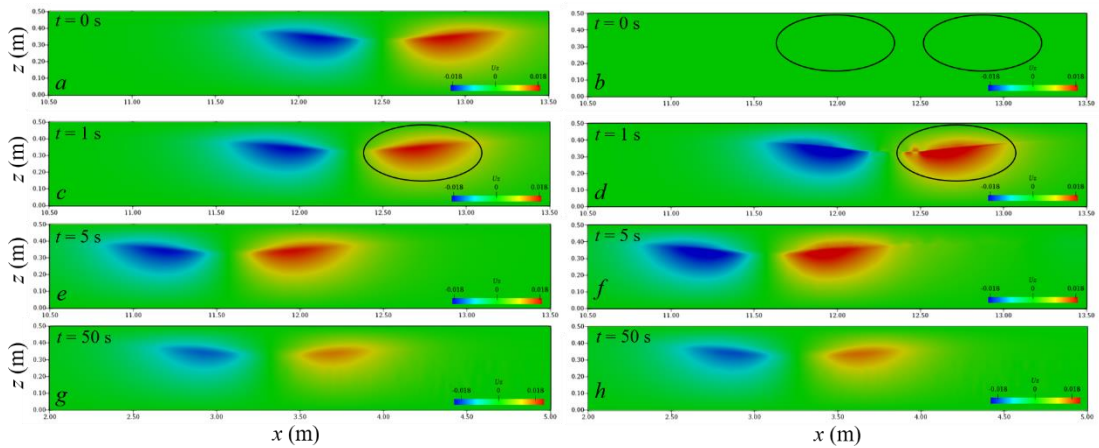
Figuire 2: Comparison chart of the vertical velocity component field: DJL equation (left) and eKdV equation (right).

The ISW propagates for 10 m, and the amplitudes of the ISWs generated by the DJL equation and the eKdV equation are reduced by 9.88% and 17.96%, respectively, as shown in Fig. 3. Overall, the reduction in energy leads to the attenuation of the amplitude of the ISW, which in turn reduces the wave speed. Except for the difference in initial fields, the grid sizes, time step, turbulence model, and other

323 features are the same. Therefore, the initial stage of ISWs generated by the eKdV equation leads to

324 excessive energy loss compared with those generated by the DJL equation. From the above analysis of

325 the velocity field, we know that the method of initializing the field with the eKdV equation requires a

326 period of movement before the jump of the velocity field develops into a field with continuous changes

327 in velocity. In addition, the DJL equation, as a fully nonlinear model, can better reflect its superiority for

328 internal waves with strong nonlinearity. Therefore, the wave generation of the subsequent numerical

329 cases in this paper adopts the method of initializing the field with the DJL equation.
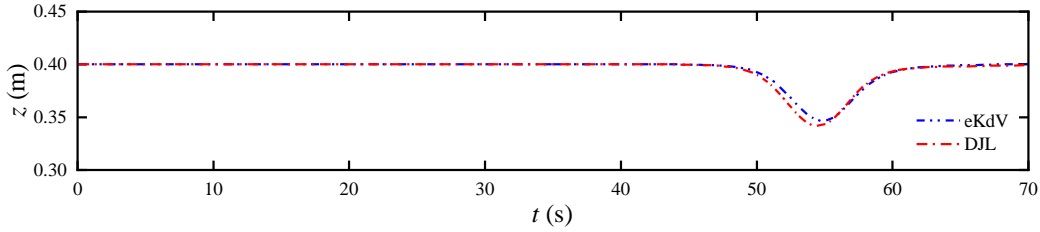
330
331 Figure 3: Time series of the interface displacement. The probe was 10 m away from the initial ISW.

332 **3. Grid independence of the ISW simulation**

333 These grid independence tests were performed in the horizontal and vertical directions by applying

334 meshes of different sizes. The sizes of the mesh determined in this paper are calculated based on the

335 amplitude of the ISW and a characteristic length determined through the integration of the wave profile

336 (Michallet and Ivey, 1999)

337
$$L = \frac{1}{a} \int_{-\infty}^{\infty} \zeta(x) dx \tag{44}$$

338 where ζ is the isopycnal vertical displacement and a is the ISW amplitude.

339 To determine the appropriate mesh size, the propagation of ISWs on flat bottoms is calculated, and

340 the numerical results are compared with the DJL theoretical solution. We set up a numerical simulation,

341 which includes a tank that is 50 m long, 0.5 m wide and has a water depth of 0.5 m. The depths of the

342 upper (h_1) and lower (h_2) layers are 0.1 m and 0.4 m, respectively, the densities of the upper and lower

343 layers are 1000 kg/m^3 and 1030 kg/m^3, respectively, the location of the centre of the pycnocline (z_{pyc}) is

344 0.4 m, and the pycnocline thickness (d_{pyc}) is 0.05 m vertically, the ISW amplitude (a) is 0.065 m. The

345 measuring point P is set at a position 10L away from the initial ISW. The sponge layer on both sides,

346 whose length is the double wave characteristic length, has been checked to properly dissipate the

347 reflected wave. Slip boundary conditions are applied to the bottom and both sides, while cyclic boundary

348 conditions are assigned to the inlet and outlet boundaries. The top boundary is a rigid lid. The boundary

349 conditions related to the density field are no-flux boundary conditions.

3.1 Grid independence in the horizontal direction

351 First, we analyse the grid independence in the horizontal direction, with a constant cell height of Δz

352 $= a/20$ m. Fig. 4 shows the results of the comparison of the waveform and decay rate in the horizontal

353 direction at probe P1 with the ISWFoam using a wide range of grid configurations. The results show a

354 negligible difference in the waveform when the mesh size is less than $L/40$, so it is difficult to accurately

355 analyse the grid independence just by the waveform. A traditional decay rate parameter is adopted,

356 namely $\delta = (a_{probe} - a_{initial})/a_{initial}$, where $a_{initial}$ is the ISW amplitude value at the initial moment, a_{probe} is

357 the ISW amplitude value of the probe $10L$ away from the initial ISW. Fig. 4(b) shows the relationship

358 between the decay rate of the ISW amplitude and the grid quantity per unit length for different mesh

359 sizes. As shown in Fig. 4(b), the decay rate of the ISW amplitude tends to be smooth as the grid number

360 per unit length increases to 160 ($\Delta x = L/150$), and then the increase in the grid quantity has a relatively

361 small effect on the decay rate. Therefore, for ISWFoam developed in this paper, we suggest that the

362 dimensions of the horizontal grid are $L/150$.
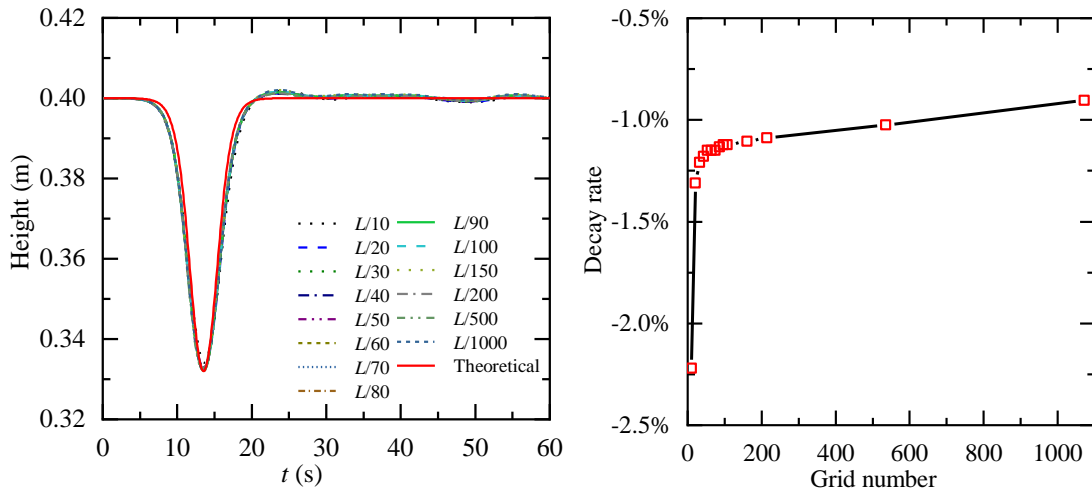
363

364 Figure 4: Grid independence in the horizontal direction at probe P1: (a) comparison of waveform and (b) decay

365 rate.

3.2 Grid independence in the vertical direction

367 Second, we analyse the grid independence in the vertical direction, with a constant cell width of Δx

368 $= L/150$ m. Fig. 5 shows the results of a comparison of the waveform and decay rate of the ISW amplitude

369 in the vertical direction at probe P1 with the ISWFoam using a wide range of grid configurations. The

370   results also show a negligible difference in the waveform when the mesh size is less than a/10, so it is

371   difficult to accurately analyse the grid independence just by the waveform. As shown in Fig. 5(b), the

372   decay rate of the ISW amplitude decreases as the grid quantity increases in a wave height range before

373   the numerical oscillation occurs. Here, we assume that the grid size with the decay rate of the ISW

374   amplitude less than one percent is the appropriate vertical grid size; namely, the vertical grid size is a/25

375   m. Therefore, for ISWFoam developed in this paper, we suggest that the dimensions of the vertical grid

376   be a/25.
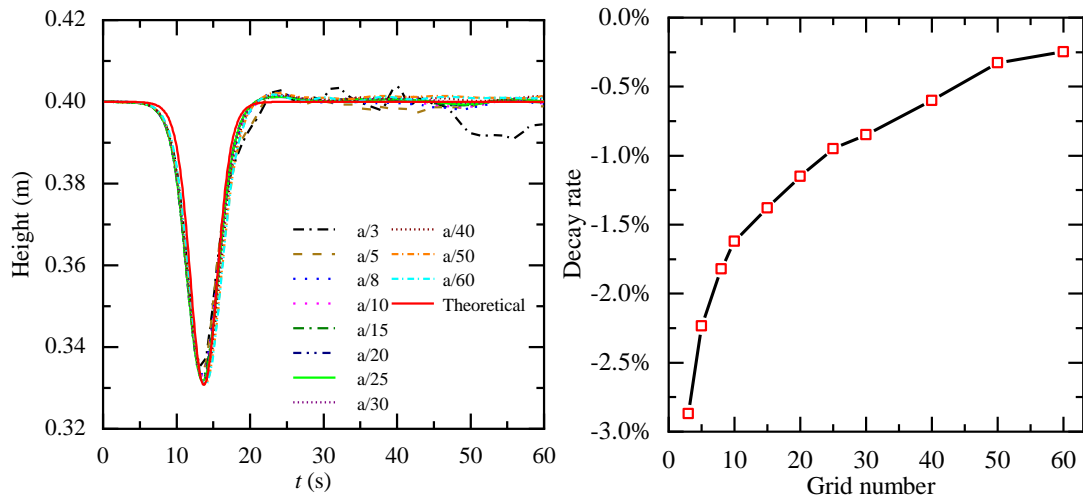
377

378   Figure 5: Grid independence analysis in the vertical direction at probe P1: (a) comparison of waveform and (b)
379   decay rate.

380   Finally, for ISWFoam developed in this paper, we suggest that the dimensions of the horizontal grid

381   are L/150, while the vertical grid is a/25.

382   **4. Model verification and results**

383   To verify the numerical model of the ISWs, the propagation of ISWs on a flat bottom section,

384   submerged triangular ridge and slopes is calculated, and the numerical results are compared with the

385   corresponding experimental results. To verify the correctness of Coriolis code implantation and reflect

386   the role of local mesh refinement, the propagation of ISWs on a flat bottom section of actual ocean scale

387   and a Gaussian ridge is calculated.

388   **4.1 ISW propagating on a flat bottom section**

389   **4.1.1 Experimental data used**

390   In this section, ISWFoam is verified by employing ISWs propagating on a flat bottom section with

391   Case Flat_4 in the continuously stratified laboratory experiment described in Hsieh et al. (2014). The

392   physical dimensions and ultrasonic probe locations in the experiments of Hsieh et al. (2014), as shown

393   in Fig. 6, are adopted to establish the numerical computation domain. We set up a numerical tank of the

394   experiment of Hsieh and co-authors, which includes a tank that is 15 m long, 0.5 m wide and has a stable

395   water depth of 0.5 m; the fluid densities of the upper (ρ_1) and lower (ρ_2) layers are 996 kg/m^3 and 1030

396   kg/m^3, respectively; the ISW amplitude (a) is 0.068 m; the location of the centre of the pycnocline (z_{pyc})

397   is 0.4 m, the pycnocline thickness (d_{pyc}) is 0.04 m vertically, and the depths of the upper (h_1) and lower

398   (h_2) layers are 0.1 m and 0.4 m, respectively. The grid is uniform in the x-direction, y-direction and z-

399   direction, and the sizes are $\Delta x = 1.5 \times 10^{-2}$ m, $\Delta y = 1.5 \times 10^{-2}$ m and $\Delta z = 2.72 \times 10^{-3}$ m, respectively. The

400   sponge layer on both sides, whose length is double wave characteristic length, has been checked to

401   properly dissipate the reflected wave. Slip boundary conditions are applied to the bottom and both sides,

402   while cyclic boundary conditions are assigned to the inlet and outlet boundaries. The top boundary is a

403   rigid lid. The boundary conditions related to the density field are no-flux boundary conditions.
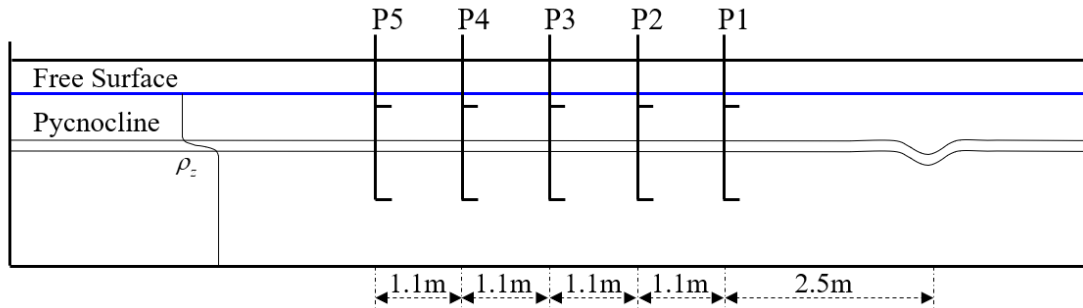
404
405   Figure 6: Schematic diagram of probe position (P1–P5) (Hsieh et al. (2014)).

406   **4.1.2 Comparisons between the numerical and experimental results**

407   Fig. 7 shows the density contours at three different times from Case Flat_4 in the laboratory

408   experiment of Hsieh and coworkers, showing the stable evolution of an ISW. The results also show the

409   realistic evolution of the thickening of the pycnocline after ISW propagation because of convection and

410   diffusion. At the same time, the propagation of the ISW is stable and unbroken.
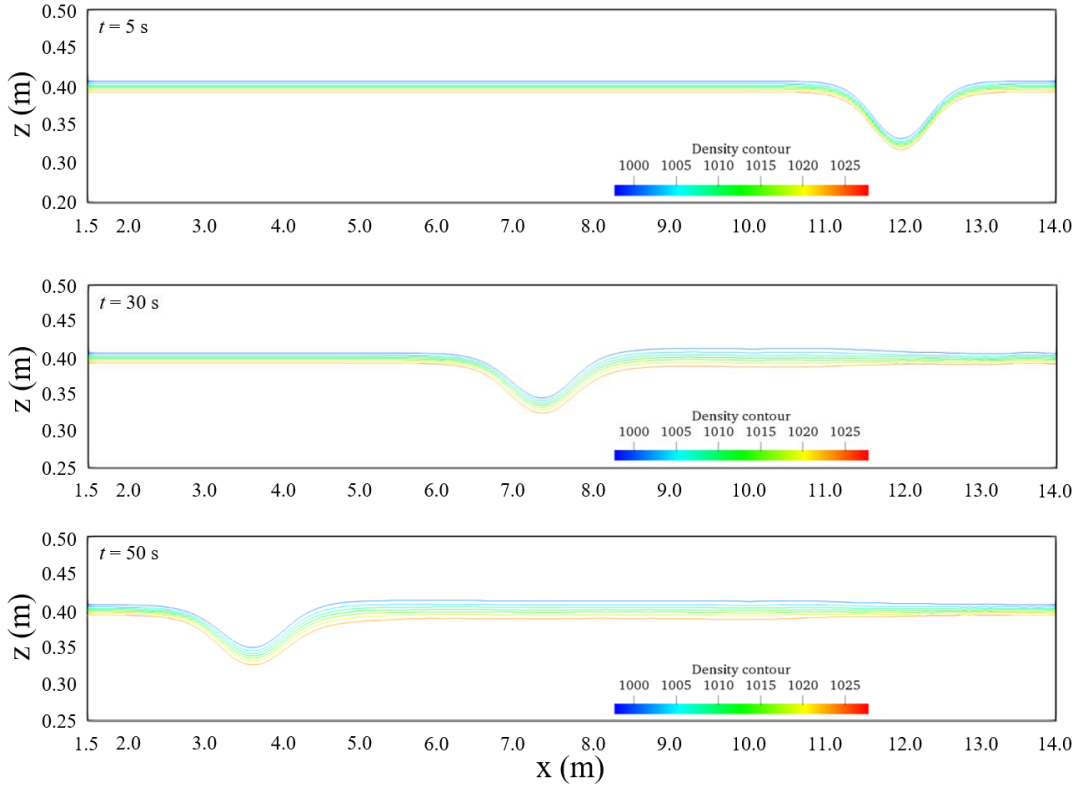
411

412

413
414

Figure 7: Density contours at different moments.

415   To further verify the model, the waveform is compared between the numerical simulations and the

416   experimental measurements, and the measurement point selection is the same as the experimental setting,

417   as shown in Fig. 6. Fig. 8 shows the comparison results between the waveform simulated by ISWFoam

418   and the experimental results at probes P1-P5. Fig. 8 shows that the results of the numerical simulations

419   agree with the experimental results (red circle). Notably, the laboratory wave height at the probe P1

420   measurement point is greater than the numerical simulation results, and the wave surface of the laboratory

421   wave is not smooth, which is caused by the wave generation method using the gravity collapse

422   mechanism in the laboratory. In general, the model developed in this paper can simulate the generation

423   and evolution of ISWs in continuously stratified fluids.
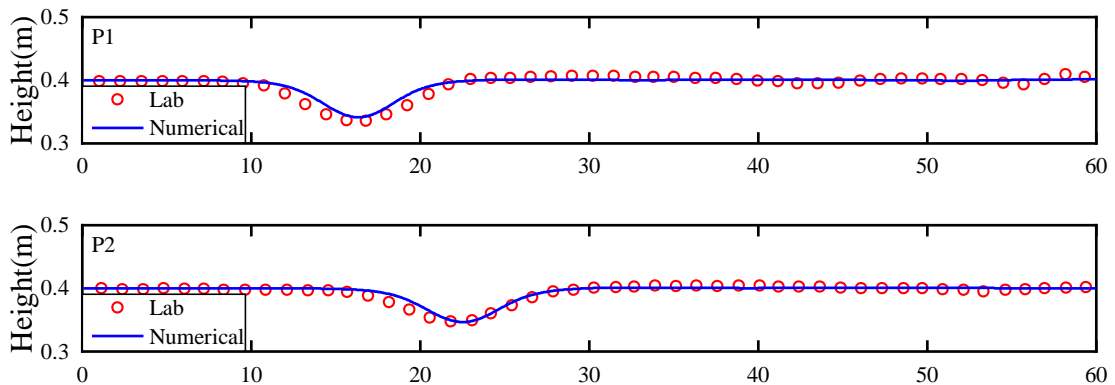
424

425
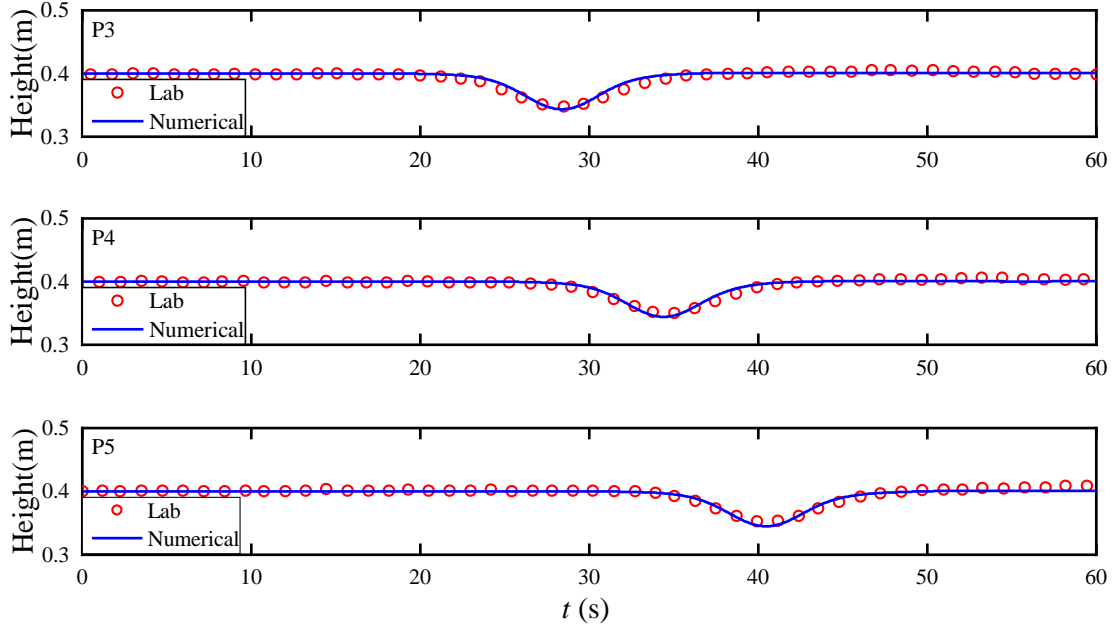
Figure 8: Comparison of the waveform between the experimental results and numerical simulation results at probes P1-P5.

4.2 ISW propagating over a submerged triangular ridge

4.2.1 Experimental data used

In this section, the validation of the numerical model is conducted through an ISW propagating over a submerged triangular ridge with the continuously stratified experiments described in Hsieh et al. (2015). The laboratory tank is 12 m long and has a stable water depth of 0.5 m, with which the fluid system has a finite thickness of the pycnocline. The specific experimental parameters used for validation of ISWFoam include the various depths of the upper (h_1) and lower (h_2) layers; the fluid density of the upper (ρ_1) and lower (ρ_2) layers of 996 kg/m^3 and 1030 kg/m^3, respectively; the ISW amplitude (α = 0.056 m); the location of the centre of the pycnocline (z_{pyc} = 0.4 m); the thickness of the pycnocline (d_{pyc} = 0.04 m vertically); the height of the isosceles triangular ridge (h_s = 0.30 m vertically); and the slope angle of the ridge for α = 45°. The physical dimensions, and ultrasonic probe locations in the experiments of Hsieh et al. (2015), as shown in Fig. 9, are adopted to establish the numerical computation domain.
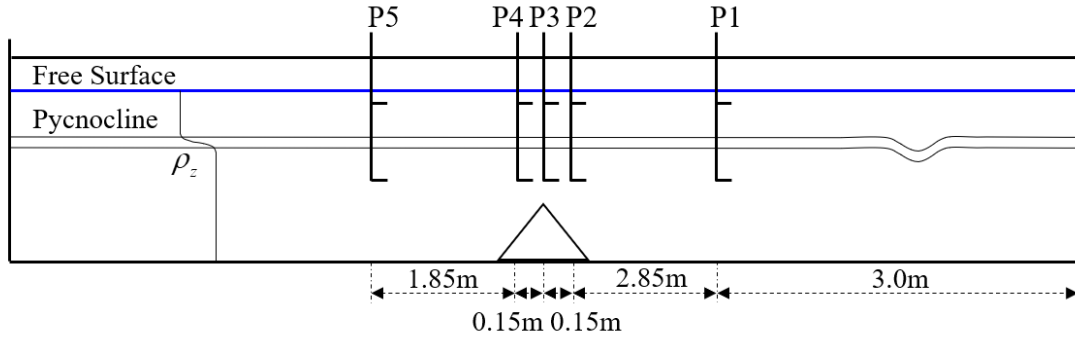
443
444   Figure 9: Schematic illustration of the laboratory setup and the locations of the probes (Hsieh et al. (2015)).

445 **4.2.2 Numerical implementation**

446   The numerical tank is designed to reproduce the experiment described in Fig. 9. The unstructured

447 grid and local mesh refinement based on the finite volume method are used to construct the computational

448 domain and discretize the governing equations. The grid is uniform in the x-direction, y-direction and z-

449 direction, and the sizes are $\Delta x = 2 \times 10^{-3}$ m, $\Delta y = 2 \times 10^{-3}$ m and $\Delta z = 2 \times 10^{-3}$ m, respectively. The precise

450 grid described triangular ridge section is $\Delta x = 2.5 \times 10^{-4}$ m, $\Delta y = 2.5 \times 10^{-4}$ m and $\Delta z = 2.5 \times 10^{-4}$ m at the

451 slope, as shown in Fig. 10. The sponge layer on both sides, whose length is double the wave characteristic

452 length defined through integration of the wave profile in Section 3 for this case, has been checked to

453 absorb the reflected wave well. A rigid wall conditions is applied to both sides, while the slip and slip

454 conditions are assigned to the bottom and the surface of the submerged ridge boundaries, respectively.

455 The top boundary is a rigid lid. The inlet and outlet boundaries adopt cyclic boundary condition. The

456 boundary conditions related to the density field are no-flux boundary conditions.
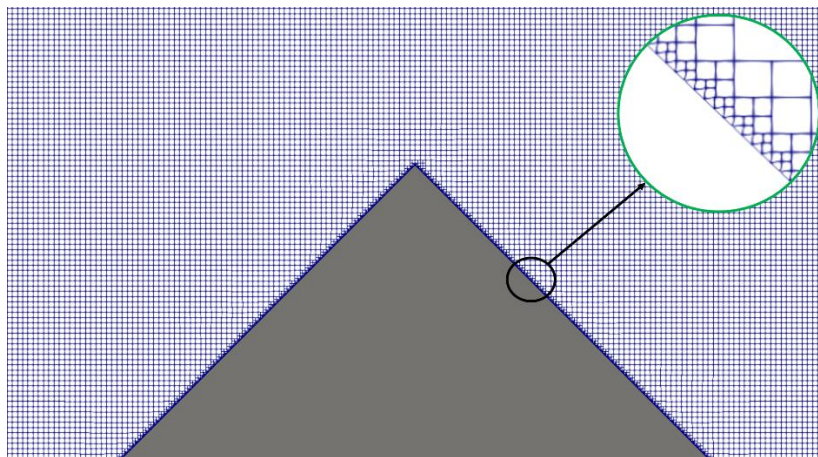
457
458   Fig. 10. Schematic of the mesh

4.2.3 Comparisons between the numerical and experimental results

Fig. 11 shows the comparison results between the waveform calculated by ISWFoam and the experimental results at probes P1-P5. In each subplot, the results of the numerical simulations (blue line) are found to be in good agreement with the experimental results (red circle). From Fig. 11 (a), the numerical simulation result of the probe P1 measurement after 20 s is different from the experimental results, which is caused by the different ISW generation methods. For the experimental results, the first large leading ISW is formed via the gravity collapse mechanism, which is trailed by a train of small-amplitude mode-one waves that is generated due to shear instabilities. However, the initialization method used to generate an initial ISW for the numerical simulation in this paper is more stable than the gravity collapse mechanism, so the rear part of the ISW is relatively flat compared to the experimental results for probe P1. In Fig. 11, the waveform of the ISW gradually evolves towards a flat waveform due to the interaction between the ISW and the ridge. In general, the model developed in this paper can simulate the interaction between ISWs and structures.
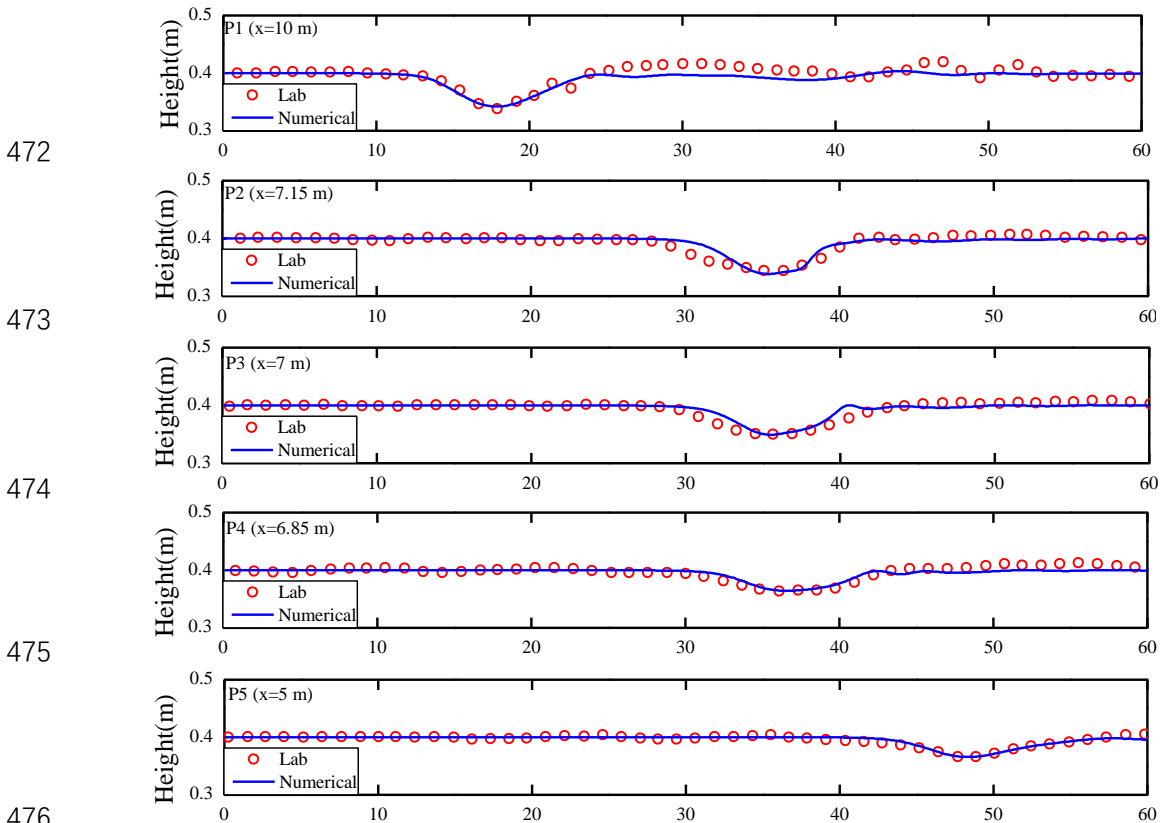
Figure 11: Comparison of the waveform between the experimental results in Hsieh et al. (2015) and numerical simulation results at probes P1-P5.

 4.3 ISW propagating on a slope

480   To verify the ability and accuracy of simulating the ISW breaking of the numerical model, two

481   continuously stratified laboratory experiments (12 and 15) of Michallet and Ivey. (1999) are chosen for

482   the simulation in this section. The experimental setup is represented schematically in Fig. 12. We set up

483   a numerical tank of the experiment of Michallet and Ivey. (1999), which includes a tank is L= 4.2 m long,

484   0.25 m wide and has a water depth of 0.15 m. The layer thickness ratio (h/H) varies from 0.60~0.91. A

485   linear slope s = 0.214 starts at 0.7 m from the right end of the tank for experiments 12 and 15. The grid

486   is uniform in the x-direction, y-direction and z-direction, and the sizes are $\Delta x = 2.5 \times 10^{-3}$ m, $\Delta y = 2.5 \times 10^{-3}$

487   ^{3} m and $\Delta z = 1.25 \times 10^{-3}$ m, respectively. The precise grid describing the slope section is $\Delta x = \Delta y = 6.25 \times 10^{-4}$

488   ^{4} m and $\Delta z = 3.125 \times 10^{-4}$ m at the slope.
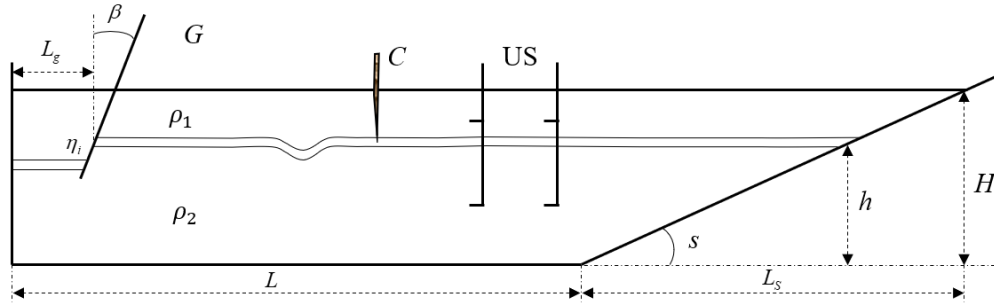
490   Figure 12: Schematic diagram of the laboratory setup. "C" and "US" represent the experimental device at probes.

491   The sponge layer on the left side, whose length is the double wave characteristic length, is checked

492   to properly dissipate the reflected wave. Slip boundary conditions are applied to the bottom and both

493   sides, while slip boundary conditions are assigned to the top boundaries. The boundary conditions related

494   to the density field are no-flux boundary conditions.

495   The vertical profile of the initial density is given by a hyperbolic tangent function profile

496
$$\overline{\rho}(z) = \rho_1 + \frac{\Delta\rho}{2}\left\{1 + \tanh\left[\frac{-\left(z - z_{pyc}\right)}{d_{pyc}}\right]\right\} \tag{45}$$

497   where z is the vertical position, $\rho_1 = 1 \times 10^3$ kg/m^3 is the base density field, $\Delta\rho$ is the change in the density,

498   z_{pyc} is the location of the centre of the pycnocline, and d_{pyc} is the thickness of the pycnocline.

499   **4.3.1 Case one and results**

500   The first case of model verification is experiment 12 of Michallet and Ivey. (1999) in this section.

501   The layer thickness ratio (h/H) is 0.84, and the density change ($\Delta\rho$) value is 14 kg/m^3. Fig. 13 presents

502   the time series for the interface displacement (ζ) for experiment 12 of Michallet and Ivey. (1999). The

503 results indicate reasonably good agreement between the time series of the simulated interface

504 displacement and that of the laboratory results. The first trough centred around *t* = 25 s represents the

505 incident ISW propagating the probe 99.8 cm away from the start of the slope. The second trough centred

506 at approximately *t* = 87 s represents the reflected ISW at the generation side, which has a smaller

507 amplitude and a longer wavelength than the incident ISW as the energy in the wave decreases. As shown

508 in Fig. 13, the smooth waveform of the incident ISW of the numerical simulation indicates that the

509 initialization method of wave generation in this paper is more stable than the experiment.
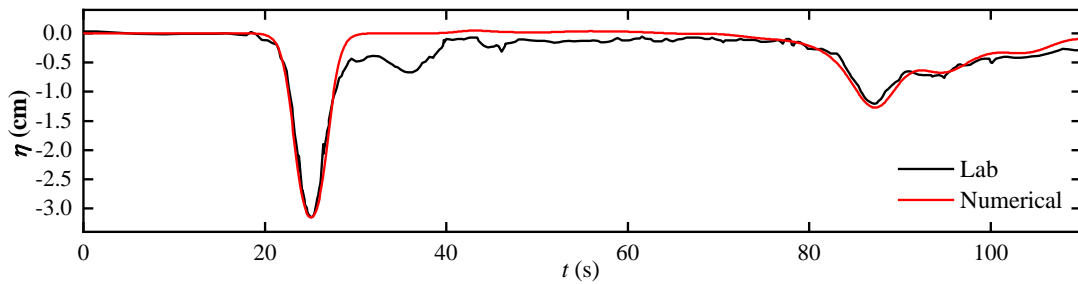
510
511 Figure 13: Time series of the interface displacement. The probe was 99.8 cm away from the start of the slope.

512 Fig. 14 shows a comparison of ISWFoam results and the experimental observations of the velocity

513 field associated with the ISW run-up process along the slope. The model effectively reproduces

514 laboratory tests, such as the intensity and direction of the velocity field, the location of the vortices, and

515 the occurrence of boundary-layer separation beneath the ISW. Therefore, the model developed in this

516 paper can reflect the ISW breaking phenomenon during the propagation of ISWs along the slope.

517

518
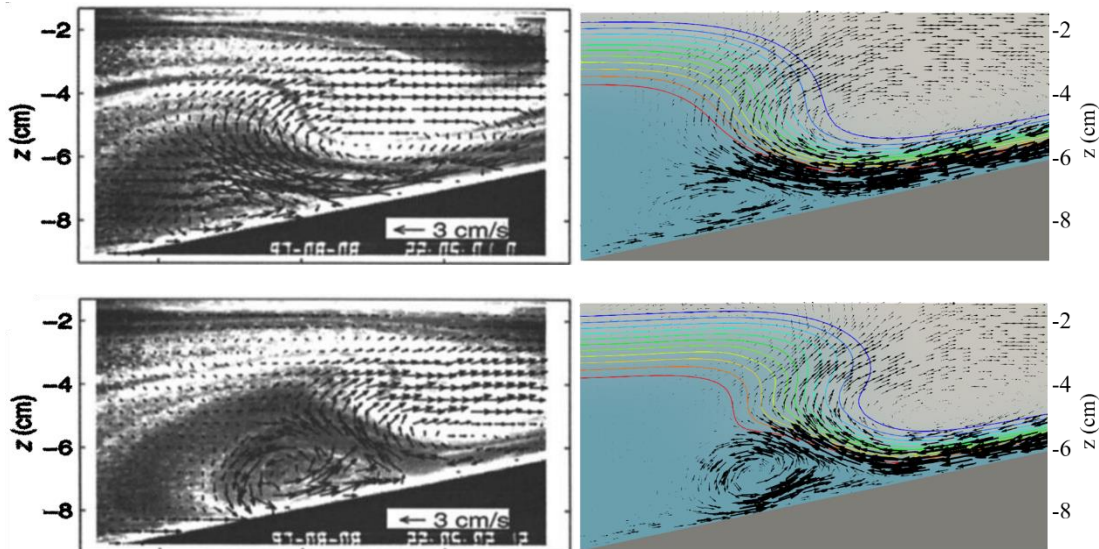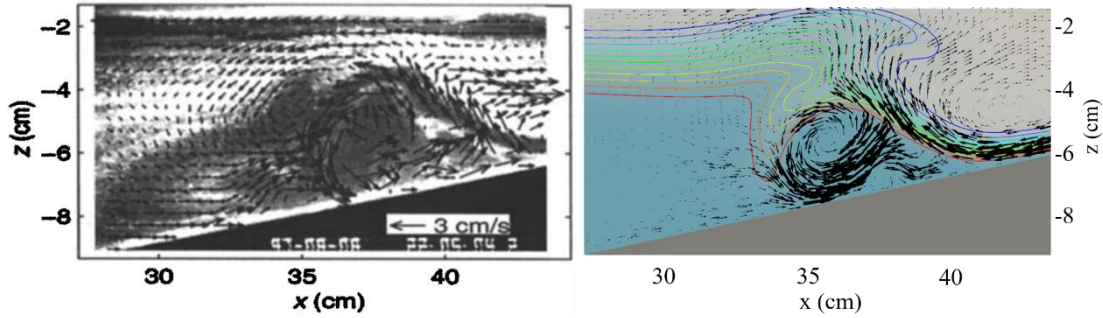
519
520 Figure 14: Comparison of the velocity field between the experimental observation results in Michallet and Ivey.
521 (1999) (left) and numerical simulation results (right).

522 **4.3.2 Case two and results**

523   Another laboratory experiment that more clearly shows the ISW breaking phenomenon from

524 Experiment 15 of Michallet and Ivey. (1999) is used to verify the numerical model presented in this paper,

525 and the corresponding numerical case is set corresponding to it. The layer thickness ratio (h/H) is 0.77,

526 and the density change ($\Delta\rho$) value is 47 kg/m^3. The wave amplitude and phase velocity at the slope

527 calculated by ISWFoam are 2.71×10^{-3} m and 10.83×10^{-1} m/s, which fit well with the experimental results

528 of 2.7×10^{-3} m and 10.8×10^{-1} m/s.

529   Fig. 15 shows the results of the numerical simulations of the ISWs propagating along the slope and

530 wave breaking using ISWFoam. As the ISW propagates to the slope, according to the conservation of

531 mass, the upper fluid forward and the downward velocity of the lower fluid increasing along the slope

532 results in the formation of a thin boundary layer, as shown in Fig. 15(*a*), (*b*), and (*c*). At the same time,

533 the amplitude of the ISW increases, and the rear of the ISW gradually becomes very steep but does not

534 overturn. With the development of the ISW, the rear waveform of the ISW cannot maintain its stability

535 and overturns forward, resulting in wave breaking, as shown in Fig. 15(*d*). After wave breaking occurs,

536 the denser lower layer flow accelerates into the less dense upper layer flow, forming a mixture region, as

537 shown in Fig. 15(*e*). After the lower layer flow is drawn downward from beneath the ISW, a mixing

538 region comprised of vortices is pushed upwards along the slope while the leading waveform is reflected,

539 as shown in Fig. 15(*f*), (*g*), and (*h*). Fig. 15(*i*), (*j*) shows the falling process of ISWs. From the perspective

540 of the entire process of wave breaking, the steepening of the rear waveform in this case is the main reason

541 for wave breaking.
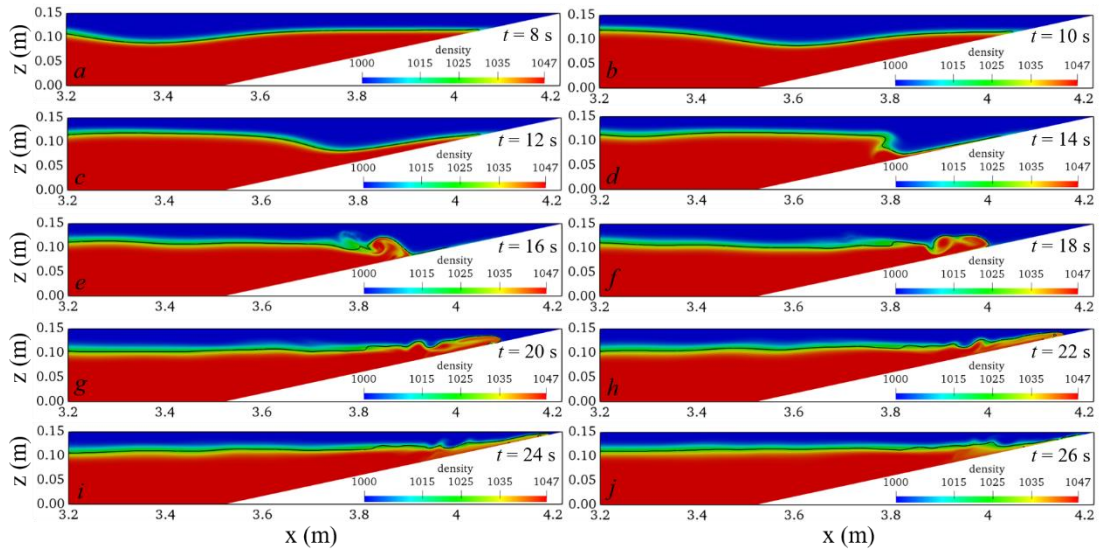
542
543 Figure 15: Temporal and spatial variations in the ISWs breaking calculated using ISWFoam (the black line
544 represents the waveform).

545 For comparison with the flow visualization image of the experiment, a specified thickness of the

546 pycnocline is presented, and the pycnocline ranges from 1003 kg/m^3 to 1045 kg/m^3 with dark colours as

547 shown in Fig. 16.

548 Fig. 16 compares the ISWFoam results and the experimental results of Michallet and Ivey. (1999)

549 before, during, and after ISW breaking. The results indicate that some main features of the laboratory

550 tests are reasonably well reproduced by ISWFoam, such as the profile of ISW, the location of the wave

551 breaking point, ISW arrival time, and spatial and temporal changes in the mixture region. Therefore, the

552 model developed in this paper can accurately simulate the ISW breaking phenomenon during the

553 propagation of ISWs along the slope.

554

555

556
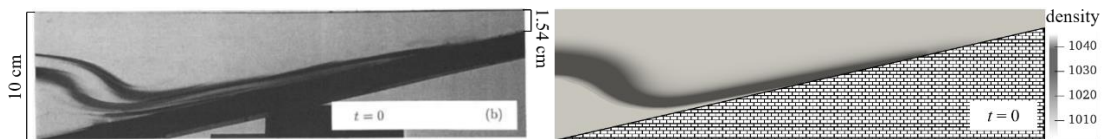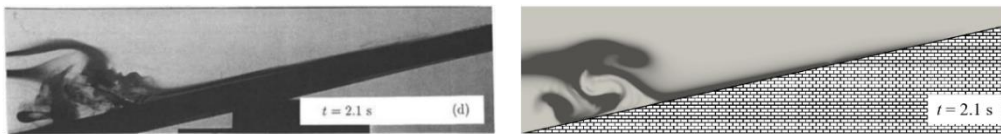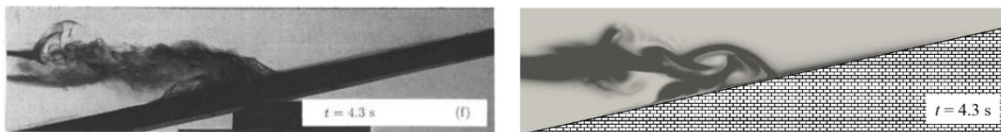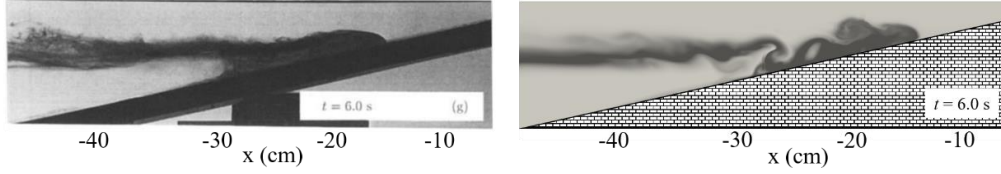
Figure 16: Comparison of the density fields between the experimental observation results in Michallet and Ivey. (1999) (left) and the numerical simulation results (right).

5. Simulation examples at the field scale

The ISWFoam model developed in the present paper can be used as a tool to investigate the interaction between ISWs and complex structures and topography. In this section, two numerical examples are presented to show the capability of ISWFoam on field scale simulation.

5.1 ISW propagating over a 3D Gaussian ridge

We designed a case of an ISW propagating over a 3D Gaussian ridge. The 3D Gaussian ridge is obtained by rotating a 2D Gaussian ridge

$$z = ae^{-(x/l)^2} \tag{46}$$

where a is the ridge amplitude, and l is the standard deviation. With $a = 100$ m and $l = 10$, we can obtain a 2D Gaussian ridge with a height of 100 m and a bottom width of 40 m. Subsequently, the 3D Gaussian ridge can be obtained after a vertical rotation of 180 degrees.

We set up a 3D numerical tank, which includes a tank that is 3 km long, 400 m wide (y-direction from -200 m to 200 m) and has a water depth of 120 m. The depths of the upper (h_1) and lower (h_2) layers are 20 m and 100 m, respectively, the densities of the upper and lower layers are 1000 kg/m^3 and 1030 kg/m^3, respectively, the location of the centre of the pycnocline (z_{pyc}) is 100 m, and the pycnocline thickness (d_{pyc}) is 1.5 m vertically, the ISW amplitude (a) is 20 m. The Gaussian ridge is located at 800 m horizontally. The grid is gradually changed from $\Delta x = 20$ m to $\Delta x = 2.5$ m in the x-direction, the grids in the y-direction are uniform with a constant cell width of $\Delta y = 2.5$ m, and the grids in the z-direction are non-uniform, with a minimum cell height of $\Delta z = 1$ m near the interface of the ISW. The precise grid described the 3D Gaussian ridge section as $\Delta x = 3.9 \times 10^{-2}$ m, $\Delta y = 3.9 \times 10^{-2}$ m and $\Delta z = 1.56 \times 10^{-2}$ m, as shown in Fig 17. The sponge layer on both sides, whose length is the double wave characteristic length, has been checked to properly dissipate the reflected wave. Slip boundary conditions are applied to the bottom and both sides, while cyclic boundary conditions are assigned to the inlet and outlet boundaries.

583   The top boundary is a rigid lid. The boundary conditions related to the density field are no-flux boundary

584   conditions.
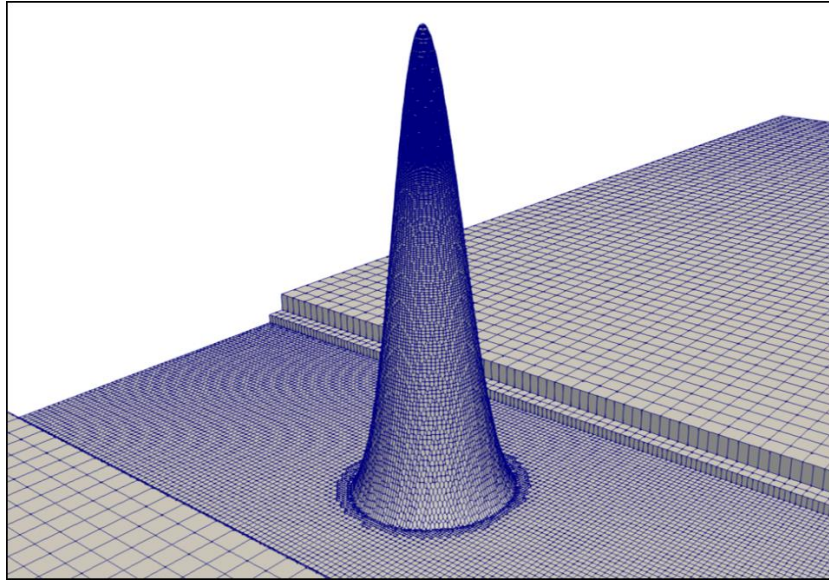
585
586   Figure 17: Schematic of the local refinement of the grid.

587   Fig. 18. shows the temporal and spatial variations in the ISWs propagating over a 3D Gaussian

588   ridge. The ISW reaches the Gaussian ridge, causing the wave surface in front of the ridge to decrease,

589   and the wave surface behind the ridge to climb up the ridge, as shown in Fig. 18(*a*). Due to being

590   obstructed by the Gaussian ridge, flow around a ridge and wave surface uplift are generated on both sides

591   of the Gaussian ridge (perpendicular to the direction of wave propagation), as shown in Fig. 18(*b*). As

592   the ISW propagated over the Gaussian ridge, the wave surface climbed along the ridge, and at the same

593   time, low velocity was generated behind the ridge, as shown in Fig. 18(*c*). Since the top of the ridge is in

594   the pycnocline, there will be a low velocity area behind the ridge for a period of time after the ISW passes,

595   as shown in Fig. 18(*d*). In general, the ISWFoam model with unstructured grids and local mesh

596   refinement can simulate the interaction between ISWs and complex structures and topography at the field

597   scale.

598
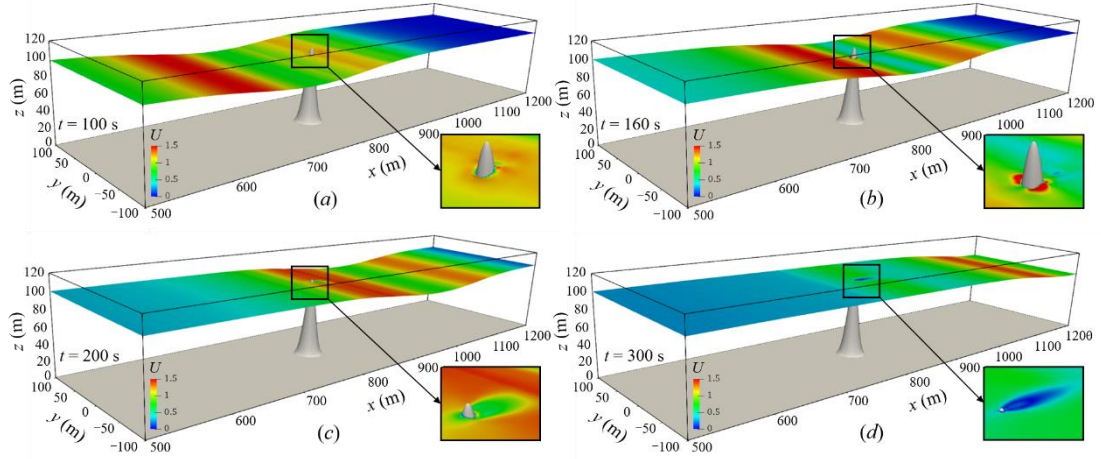
599 Figure 18: Temporal and spatial variation in the ISWs propagating over a 3D Gaussian ridge.

600 **5.2 ISW propagating over a hyperbolic tangent terrain**

601 The propagation of ISWs to the shore is bound to be affected by the continental shelf, and

602 shallow water evolution phenomena such as nonlinear evolution, breaking phenomenon and

603 waveform inversion occur on the undulating continental shelf. For simplicity, this section simplifies

604 the continental shelf into a hyperbolic tangent terrain, the terrain profile formula is as follows (Lamb,

605 2002)

606
$$z = \frac{a_T}{2}\left(1 + \tanh\left(\frac{x}{L}\right)\right) \tag{47}$$

607 where a_T is the ridge amplitude, which is 60 m, and l is the width of the continental shelf change area,

608 which is 200 m, and x and z are the horizontal and vertical coordinate positions, respectively.

609 We set up a 3D numerical tank, which includes a tank that is 7.5 km long, 200 m wide (y-direction

610 from -100 m to 100 m) and has a water depth of 100 m (z-direction from 0 m to 100 m). The depths of

611 the upper (h_1) and lower (h_2) layers are 20 m and 80 m in the deep water, respectively, and the depths of

612 the upper (h_1) and lower (h_2) layers are both 20 m in the shallow water. The densities of the upper and

613 lower layers are 1000 kg/m³ and 1012 kg/m³, respectively, and the pycnocline thickness (d_{pyc}) is 2 m, the

614 location of the pycnocline (z_{pyc}) centre is at 80 m, the ISW amplitude (a) is 20 m. The starting point of

615 the hyperbolic tangent terrain is located at 0 m horizontally, and the top of the terrain is 40 m underwater.

616 Therefore, ISWs will gradually propagate from deep water area with a water depth of 100 m to shallow

617 water area with a water depth of 40 m. The horizontal grid is gradually changed from 40 m at the inlet to

618   4 m in the study area, and then from the study area to 60 m at the outlet, the grid is uniform in the y-

619   direction and z-direction, which are 4 m and 1 m. The hyperbolic tangent terrain is characterized by 4-

620   level local mesh refinement, and the minimum grid size is 5 cm, as shown in Fig 19. The sponge layer

621   on both sides, whose length is the double wave characteristic length, has been checked to properly

622   dissipate the reflected wave. Cyclic boundary conditions are assigned to the inlet, outlet and both sides,

623   while the slip and non-slip conditions are assigned to the bottom and the shelf topography. The top

624   boundary is a rigid lid. The boundary conditions related to the density field are no-flux boundary

625   conditions.
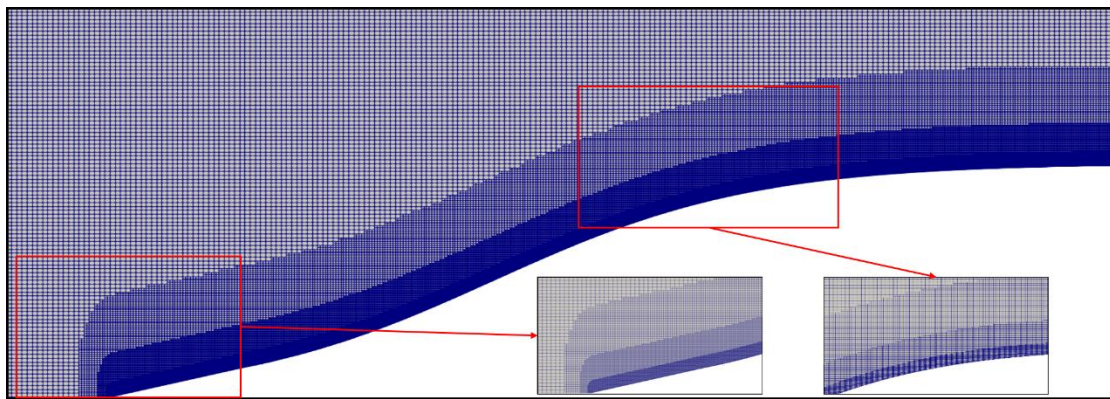
626

627 Figure 19: Schematic of the local refinement of the grid.

628   Fig. 20. shows the waveform and velocity field when the ISW passes through the hyperbolic tangent

629   terrain. From Fig. 20, it can be seen that the ISW breaks and has a significant waveform inversion when

630   propagating from deep water of 100 m to shallow water of 40 m. As the ISWs propagate to the continental

631   shelf, the water depth gradually becomes shallower, and the thickness of the lower fluid gradually

632   decreases as shown in Fig. 2-20(a). Due to the presence of the continental slope, the nonlinearity of the

633   ISWs becomes stronger, and the trough velocity of the ISWs is significantly lower, which causes the

634   waveform at the rear of the ISW to become steep, as shown in Fig. 2-20(b). At the same time, the front

635   waveform of the ISW gradually becomes flat and parallel to the shelf topography. As the waveform at

636   the rear of the ISW becomes steeper and loses balance, the waveform at the rear of the ISW rolls forward,

637   leading to the occurrence of ISW breaking phenomenon, as shown in Fig. 2-20(c). It is worth noting that

638   the ISW breaking occurs at the rear of the ISW, while the front waveform does not break, but transforms

639   into another form of wave (referred to as the head wave), and continues to propagate steadily along the

640   continental shelf. The breaking of ISWs causes severe disturbances in the water, and excite a series of

641   secondary waves at the tail of the head wave, represented by elevation ISWs (as shown in Fig. 2-20(d),

642   (e), (f)), and then elevation ISWs propagate forward steadily in shallow water (as shown in Fig. 2-20(g),

643   (h), (i)). The shelf slope of the case in this section is the same as the shelf slope of s8_c1c case studied

by Lamb and Xiao (2014), both of which are 0.1. The research results of Lamb and Xiao (2014) show that waveform inversion of a depression ISW will occur at this shelf slope, and a series of elevation ISWs will be generated and propagate stably in shallow water. The simulated results have good agreement with that of Lamb and Xiao (2014).

654

655

656
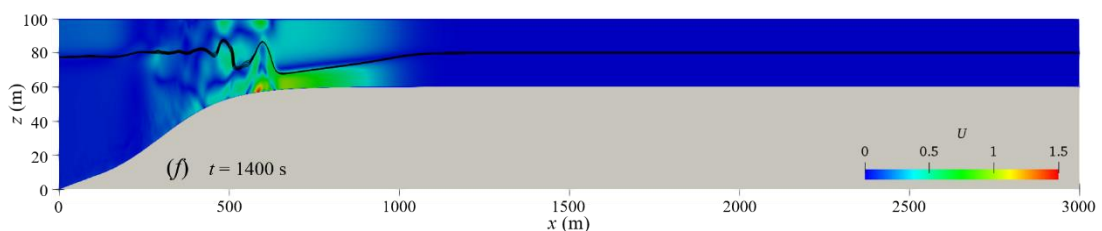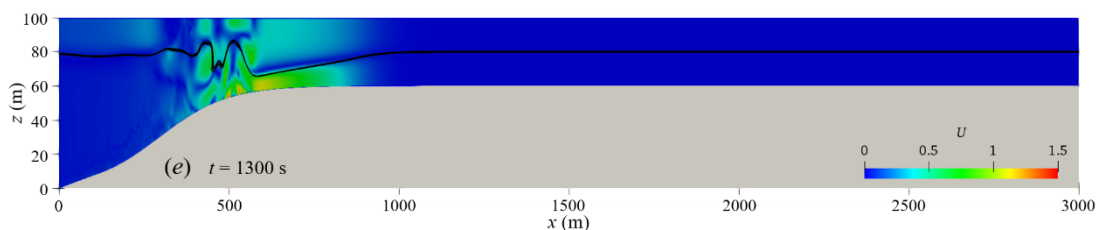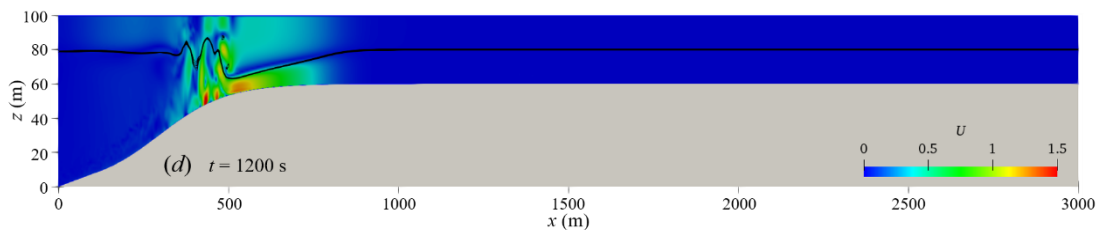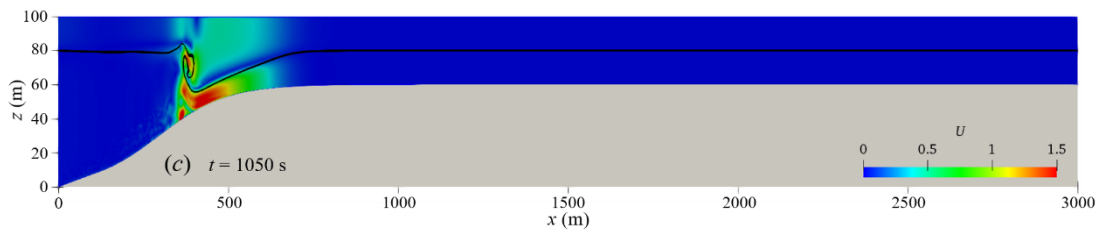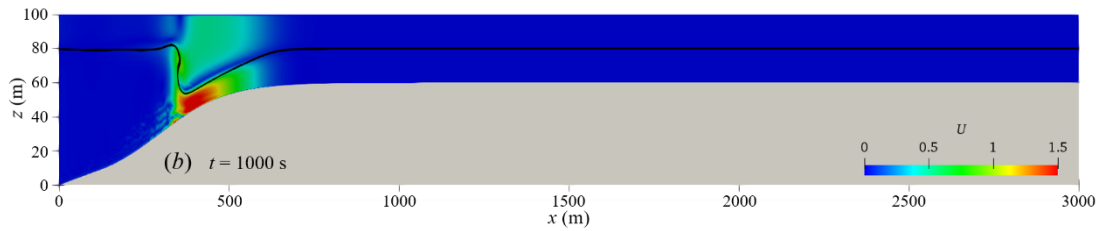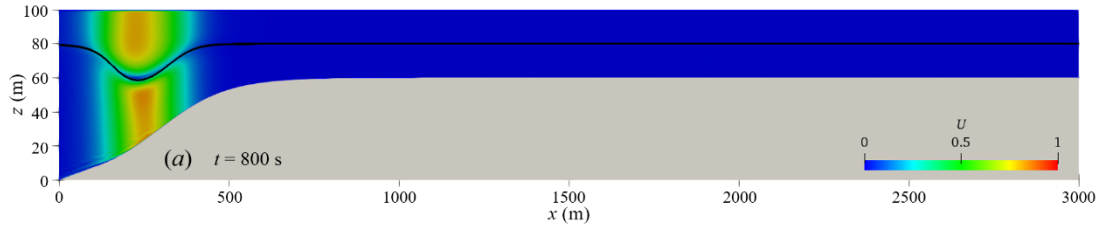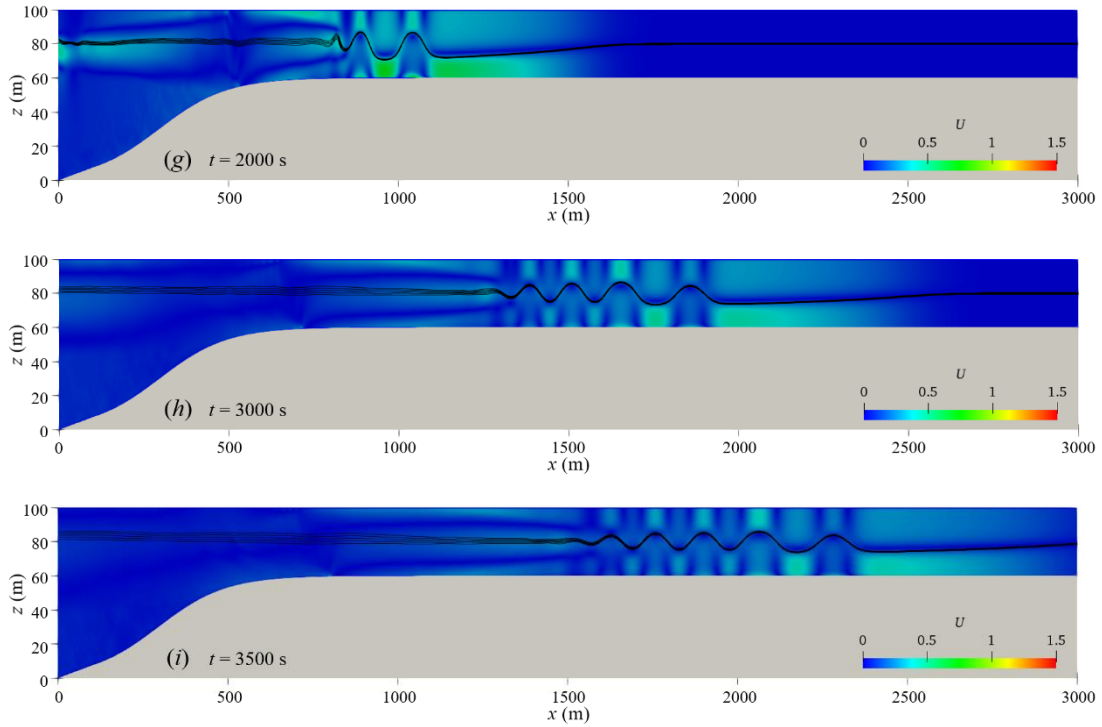
657 Figure 20: Velocity field diagram of ISW propagation (the black solid line is the iso-density contours).

658 The vortex structure has an important influence on the material transport at the bottom of the shelf,

659 so it is very necessary to study the vortex structure when the ISW breaks. Fig. 2-21 shows the vorticity

660 field of the ISW at the breaking stage. With the occurrence of ISW breaking, a significant

661 counterclockwise vortex structure is generated below the waveform at the rear of the ISW, as shown in

662 Fig. 2-21(a). With the propagation of the head wave, the vortex climbs along the shelf, and the vortex

663 continues to develop horizontally and vertically during the upward climb, and the vertical scale is about

664 1/3 of the local water depth (as shown in Fig. 2-20(b), (c)). As the vortex structure continues to climb,

665 the vorticity decays, and the vortex structure gradually disappears, as shown in Fig. 2-21(d), (e).

666 Combined with the velocity field in Fig. 2-20, it can be seen that the vorticity before and after the ISW

667 breaks is the largest, and the vortex structure is the most obvious. As the wave train of elevation ISWs

668 propagates steadily, the vortex structure climbs up the shelf and gradually disappears.

669
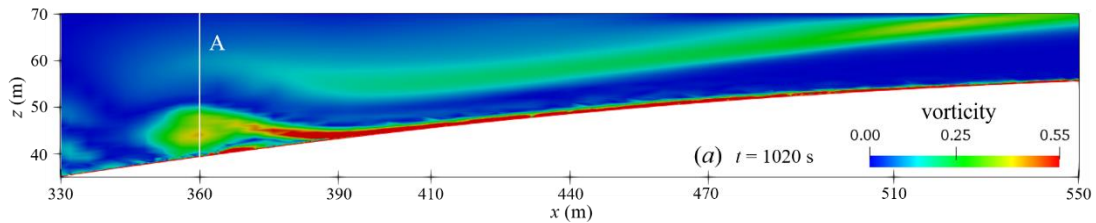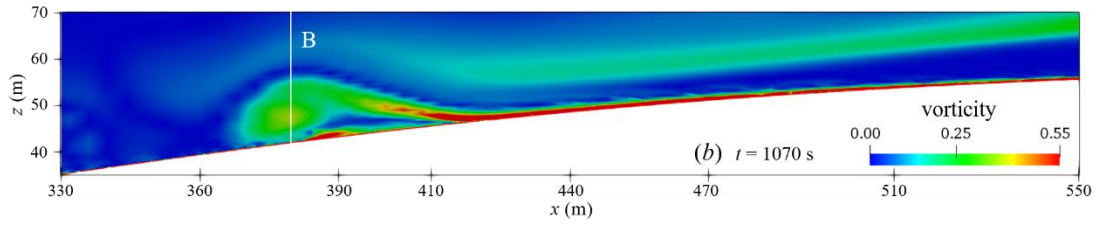
670
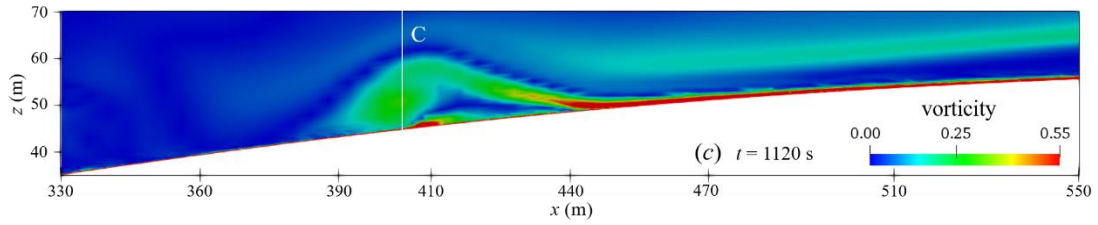
671
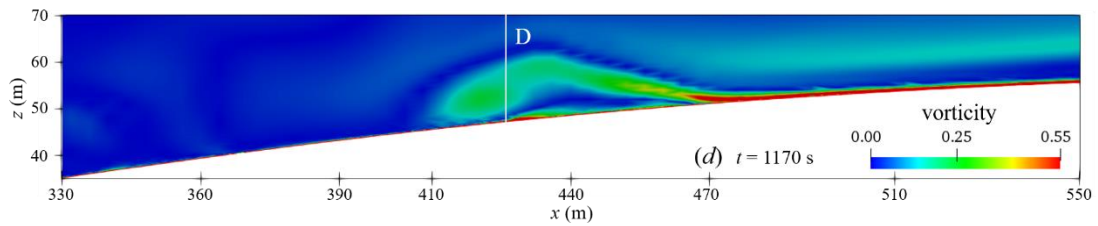
672
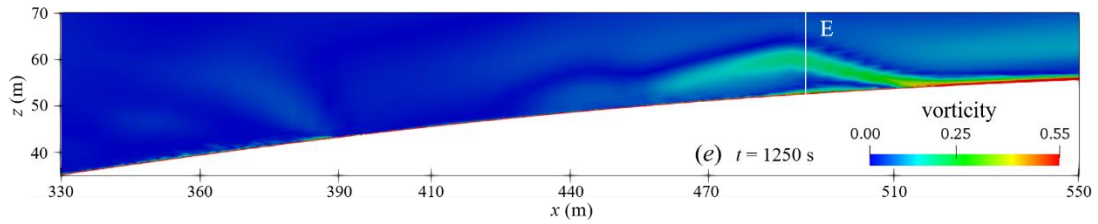
673

674 Figure 21: Vorticity field (A-E represents transverse section)

675   In order to analyze the vortex of the three-dimensional structure, Fig. 2-22 shows the vorticity

676 field diagram on the transverse section, and the position of the transverse section corresponds to the

677 marked section in Fig. 2-21. It can be seen from Fig. 2-22 that the vortex also evolves in the

678 transverse section. Obviously, the bottom vortex structure generated by ISW breaking shows three-

679 dimensional non-uniform features.

680

681

682

683

684

685 Figure 22: Vorticity field of transverse section.

686   The velocity vector field of the head wave and the wave train of elevation ISWs in the shallow

687 water area are shown in Figure 2-23. The head wave generated by the breaking of the ISW loses the

688 original wave shape of the ISW, the wave height becomes smaller, the wavelength becomes longer,

689 and the velocity field is still in the form of upper layer forward and lower layer backward (as shown

690 in Fig. 2-23(a), (b)). In Fig. 2-23(c), (d), the velocity field and waveform of the entire wave train

691 following the head wave are stable, and the velocity field of each wave is backwards in the upper

692 layer and forwards in the lower layer, and the wavelength gradually becomes longer as the wave

693 train propagates. As the wave train propagates in shallow water, there is a large vorticity in the crest

694 and trough areas of each wave, and it propagates forward steadily as the wave train propagates, as

695 shown in Fig. 2-24. Generally, the waveform inversion and breaking phenomenon of ISWs is well

696 indicated, and the propagation and evolution of the wave train generated by waveform inversion is

697 also accurately described through ISWFoam simulation.

698

699
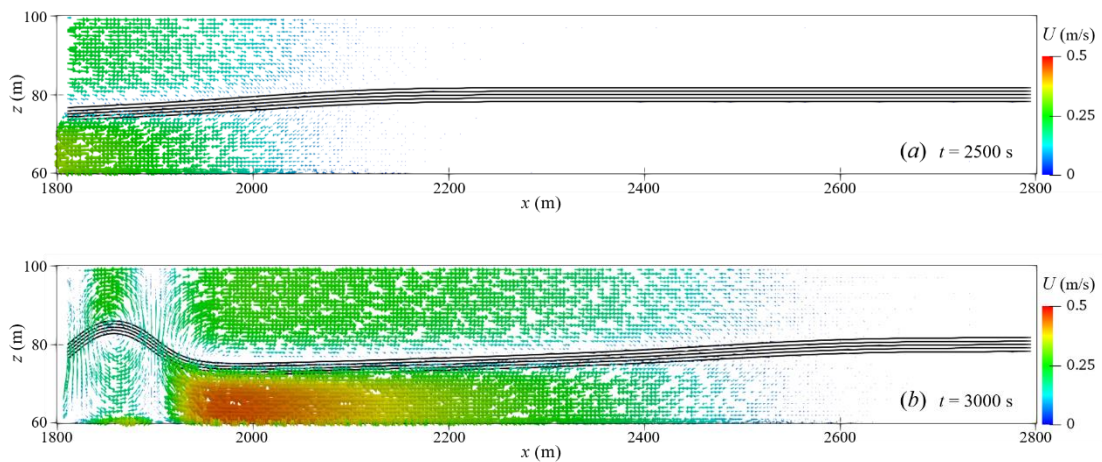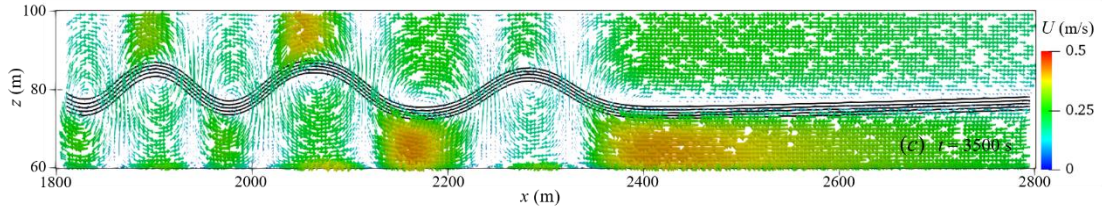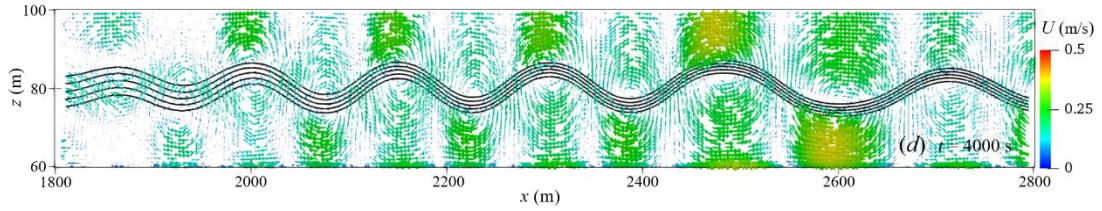
Figure 23: Velocity vector field of wave train in shallow water area.
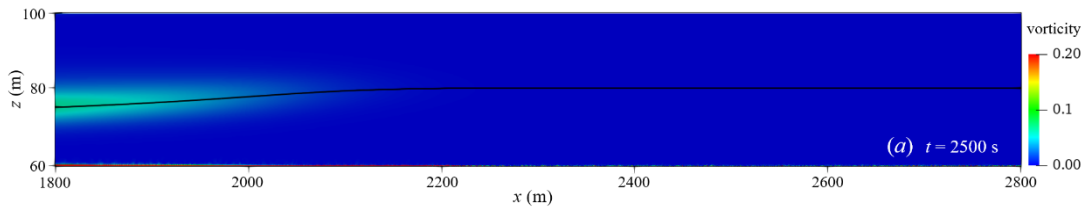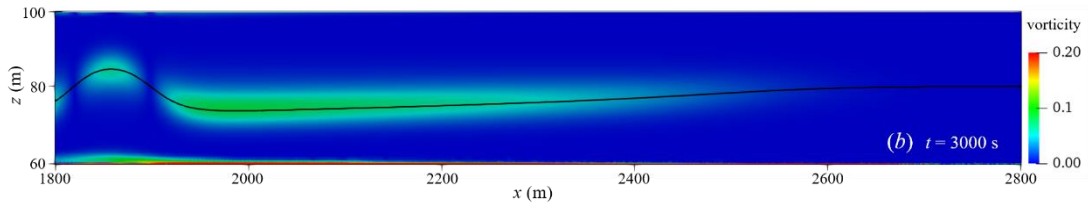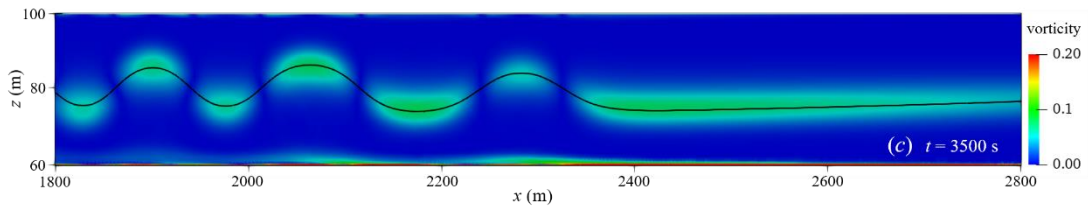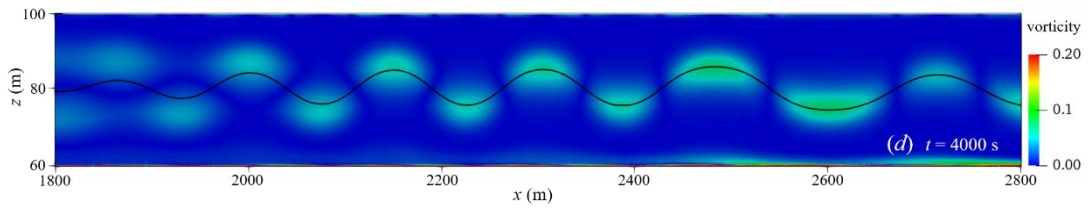
Figure 24: Vorticity field of wave train in shallow water (the black solid line is the waveform).

6. Conclusions

In this paper, a numerical model referred to as ISWFoam with a modified *k-ω SST* model, established by combining the density transport equation with a fully three-dimensional (3D) Navier-

Stokes equation, is developed to simulate ISWs in continuously stratified, incompressible, viscous fluids based on the finite volume method with unstructured grids and local mesh refinement of OpenFOAM. ISWFoam provides two initial wave generation methods to generate an ISW in continuously stratified fluids, including solving the weakly nonlinear models of the eKdV equation and the fully nonlinear models of the DJL equation. The verification process presents several applications, such as ISWs propagating on flat bottoms including laboratory scale and actual ocean scale, and ISWs over a submerged triangular ridge, a Gaussian ridge and slopes. The following conclusions were obtained as a result of this study.

ISWFoam using the finite volume method with unstructured grids and local mesh refinement can accurately simulate the generation and evolution of ISWs, the ISW breaking phenomenon, waveform inversion of ISWs and the interaction between ISWs and complex structures and topography. The method of initializing the ISW using weakly nonlinear eKdV equation models requires a period of movement before the jump of the velocity field develops into a field with continuous changes in velocity. The DJL equation wave generation method that considers the vertical velocity and the horizontal velocity along the vertical gradient is better than the eKdV equation wave generation method that only provides the horizontal average velocity. Using ISWFoam to simulate an ISW with infinite wave length, the metric for the appropriate mesh size is given as follows: the dimensions of the horizontal grid are one-one hundred and fiftieth of the characteristic length, while the vertical grid takes one-twenty fifth of the ISW amplitude.

Computer code availability

The ISWFoam code (DOI:10.5281/zenodo.5069480.) developed in this article can be downloaded for free from https://zenodo.org/record/5069480#.YU1j_GJByHs.

Author contributions

QZ and JL jointly developed this numerical method to calculate internal solitary waves in continuously stratified fluids. JL developed the code. TC performed the computations. QZ and JL jointly analysed the calculation results and wrote the paper together.

738 **Competing interest**

739   The authors of this paper declare that they have no conflicts of interest.

740 **Financial support**

741   This work is supported by grants from the National Key Research and Development Program of

742 China (2017YFC1404200), and the National Natural Science Foundation of China (51509183).

743 **Reference**

Alford, M. H., Lien, R. C., Simmons, H., Klymak, J., Ramp, S., Yang, Y. J., Tang, D., and Chang, M. H.: Speed and evolution of nonlinear internal waves transiting the South China Sea, Journal of Physical Oceanography., 40, 1338-1355, doi:10.1175/2010JPO4388.1, 2010.

Alford, M. H., MacKinnon, J. A., Nash, J. D., Simmons, H., Pickering, A., Klymak, J. M., Beitzel, T.: Energy flux and dissipation in Luzon Strait: Two tales of two ridges, Journal of Physical Oceanography., 41, 2211-2222. doi:10.1175/JPOD11073.1, 2011.

Alford, M. H., Peacock, T., MacKinnon, J. A., Nash, J. D., Buijsman, M. C., Centurioni, L. R., Fu, K. H.: The formation and fate of internal waves in the South China Sea, Nature., 521, 65-69, doi:10.1038/nature14399, 2015.

Aghsaee, P., Boegman, L., Lamb, K. G.: Breaking of shoaling internal solitary waves, Journal of Fluid Mechanics., 659, 289. doi:10.1017/S002211201000248X, 2010.

Aghsaee, P., Boegman, L., Diamessis, P. J., Lamb, K. G.: Boundary-layer-separation-driven vortex shedding beneath internal solitary waves of depression, Journal of Fluid Mechanics., 690, 321, doi:10.1017/jfm.2011.432, 2012.

Apel, J., Ostrovsky, L., Stepanyants, Y., Lynch, J.F.: Internal Solitons in the Ocean, Technical Report Woods Hole Oceanographic Institution., doi:10.1575/1912/1070, 2006.

Bardina, J.E., Coakley, T.J., and Huang, P.G.: Turbulence Modeling Validation, Testing, and Development, NASA TM 110446, NASA Ames Research Center, Moffett Field, Calif. doi: 10.2514/6.1997-2121, 1997.

Bell, J. B. and Marcus, D. L.: A second-order projection method for variable-density flows, Journal of Computational Physics., 101(2), 334-348, doi:10.1016/0021-9991(92)90011-M, 1992.

Brown, D. J. and Christie, D. R.: Fully nonlinear solitary waves in continuously stratified incompressible Boussinesq fluids, Physics of Fluids., 10(10), 2569-2586, doi:10.1063/1.869771, 1998.

Boegman, L. and Stastna, M.: Sediment resuspension and transport by internal solitary waves, Annual review of fluid mechanics., 51, 129-154, doi:10.1146/annurev-fluid-122316-045049, 2019.

Buijsman, M. C., McWilliams, J. C., and Jackson, C. R.: East-west asymmetry in nonlinear internal waves from Luzon Strait, Journal of Geophysical Research: Oceans., 115(C10),

doi:10.1029/2009JC006004, 2010.

Cai, S., Xie, J., and He, J.: An overview of internal solitary waves in the South China Sea, Surveys in Geophysics., 33, 927-943, doi:10.1007/s10712-012-9176-0, 2012.

Cheng, M. H., Hwang, R. R., and Hsieh, C. M.: Numerical study on the transformation of an internal solitary wave propagating across a vertical cylinder, Applied Ocean Research., 95, 102016, doi:10.1016/j.apor.2019.102016, 2020.

Choi, W. and Camassa, R.: Fully nonlinear internal waves in a two-fluid system, Journal of Fluid Mechanics., 396, 1-36, doi:10.1017/S0022112099005820, 1999

Deshpande, S. S., Anumolu, L., and Trujillo, M. F.: Evaluating the performance of the two-phase flow solver interFoam, Computational Science. Discovery 5, 014016, 1-36, doi:10.1088/1749-4699/5/1/014016, 2012.

Diamessis, P. J., Domaradzki, J. A., and Hesthaven, J. S.: A spectral multidomain penalty method model for the simulation of high Reynolds number localized incompressible stratified turbulence, Journal of Computational Physics., 202(1), 298-322, doi:10.1016/j.jcp.2004.07.007, 2005.

Ding, W., Ai, C., Jin, S., Lin, J.: Numerical investigation of an internal solitary wave interaction with horizontal cylinders, Ocean Engineering., 208, 107430, doi:10.1016/j.oceaneng.2020.107430, 2020.

Dunphy, M., Subich, C., and Stastna, M.: Spectral methods for internal waves: indistinguishable density profiles and double-humped solitary waves, Nonlinear Processes in Geophysics., 18(3), 351-358, doi:10.5194/npg-18-351-2011, 2011.

Farmer, D. M.and Smith, J. D.: Tidal interaction of stratified flow with a sill in Knight Inlet, Deep Sea Research Part A. Oceanographic Research Papers., 27(3-4), 239-254, doi:10.1016/0198-0149(80)90015-1, 1980.

Fringer, O. B., Gerritsen, M., and Street, R. L.: An unstructured-grid, finite-volume, nonhydrostatic, parallel coastal ocean simulator, Ocean Modelling., 14(3-4), 139-173, doi:10.1016/j.ocemod.2006.03.006, 2006.

Fu, D. M., You, Y. X., and Li, W., Numerical simulation of internal solitary waves with a submerged body in a two-layer fluid, Ocean Engineering (Haiyang Gongcheng)., 37(3), 38-44, 2009.

Gao, X. Y., You, Y. X., Wang, X., Li, W.: Numerical simulation for the internal solitary wave based on MCC theory, Ocean Engineering (Haiyang Gongcheng)., 30(4), 29-36, 2012.

Grimshaw, R., Pelinovsky, E., Talipova, T., Kurkina, O.: Internal solitary waves: propagation, deformation and disintegration, Nonlinear Processes in Geophysics., 17(6), 633-649, doi:10.5194/npg-17-633-2010, 2010.

Guo, C. and Chen, X.: A review of internal solitary wave dynamics in the northern South China Sea, Progress in Oceanography., 121, 7-23, doi:10.1016/j.pocean.2013.04.002, 2014.

Hallberg, R. and Rhines, P.: Buoyancy-driven circulation in an ocean basin with isopycnals intersecting the sloping boundary, Journal of Physical Oceanography., 26(6), 913-940, doi:10.1175/1520-0485(1996)026<0913:BDCIAO>2.0.CO;2, 1996.

Hallberg, R.: Stable split time stepping schemes for large-scale ocean modeling, Journal of

Computational Physics., 135(1), 54-65, doi:10.1006/jcph.1997.5734, 1997.

Helfrich, K. R. and Melville, W. K.: Long nonlinear internal waves, Annu. Rev. Fluid Mech., 38, 395-425, doi:10.1146/annurev.fluid.38.050304.092129, 2006.

Hsieh, C. M., Hwang, R. R., Hsu, J. R. C., Cheng, M. H.: Flow evolution of an internal solitary wave generated by gravity collapse, Applied Ocean Research., 48, 277-291, doi:10.1016/j.apor.2014.10.001, 2014.

Hsieh, C. M., Hwang, R. R., Hsu, J. R. C., Cheng, M. H.: Numerical modeling of flow evolution for an internal solitary wave propagating over a submerged ridge, Wave Motion., 55, 48-72, doi:10.1016/j.wavemoti.2014.12.008, 2015.

Hibiya, T.: The generation of internal waves by tidal flow over Stellwagen Bank, Journal of Geophysical Research: Oceans., 93, 533-542, doi:10.1029/JC093iC01p00533, 1988.

Hu, H. C., Tong, B. and Lou, S. Y.: Nonsingular positon and complexiton solutions for the coupled KdV system, Physics Letters A., 351, 403-412, doi:10.1016/j.physleta.2005.11.047, 2006.

Huthnance, J. M.: Waves and currents near the continental shelf edge, Progress in Oceanography., 10, 193-226, doi:10.1016/0079-6611(81)90004-5, 1981.

Issa, R. I.: Solution of the implicitly discretised fluid flow equations by operator-splitting, Journal of computational physics., 62(1), 40-65, doi:10.1016/0021-9991(86)90099-9, 1986.

Jasak, H.: Error Analysis and Estimation for the Finite Volume Method with Applications to Fluid Flows, Ph.D. thesis. Imperial College London, 1996.

Ko, D. S., Martin, P. J., Rowley, C. D., Preller, R. H.: A real-time coastal ocean prediction experiment for MREA04, Journal of Marine Systems., 69(1-2), 17-28, doi:10.1016/j.jmarsys.2007.02.022, 2008.

Kubota, T., Ko, D. R. S., and Dobbs, L. D.: Weakly-nonlinear, long internal gravity waves in stratified fluids of finite depth, Journal of Hydronautics., 12, 157-165, doi:10.2514/3.63127, 1978.

Lamb, K. G.: Numerical experiments of internal wave generation by strong tidal flow across a finite amplitude bank edge, Journal of Geophysical Research: Oceans., 99, 843-864, doi:10.1029/93JC02514, 1994.

Lamb, K. G. and Yan, L.: The evolution of internal wave undular bores: comparisons of a fully nonlinear numerical model with weakly nonlinear theory, Journal of physical oceanography., 26(12), 2712-2734, doi:10.1175/1520-0485(1996)026<2712:TEOIWU>2.0.CO;2, 1996.

Lamb, K. G.: A numerical investigation of solitary internal waves with trapped cores formed via shoaling. Journal of Fluid Mechanics, 451, 109-144, doi.org/10.1017/S002211200100636X, 2002.

Lamb, K. G. and Nguyen, V. T.: Calculating energy flux in internal solitary waves with an application to reflectance, Journal of Physical Oceanography., 39, 559-580, doi:10.1175/2008JPO3882.1, 2009.

Lamb, K. G.: Energy and pseudoenergy flux in the internal wave field generated by tidal flow over topography, Continental Shelf Research., 27, 1208-1232, doi:10.1016/j.csr.2007.01.020, 2007.

Lamb K G, Xiao W.: Internal solitary waves shoaling onto a shelf: Comparisons of weakly-nonlinear and fully nonlinear models for hyperbolic-tangent stratifications, Ocean Modelling., 78, 17-34,

doi.org/10.1016/j.ocemod.2014.02.005, 2014.

Li, J. Y., Zhang, Q. H., and Chen. T. Q.: Numerical Simulation of Internal Solitary Wave in Continuously Stratified Fluid, Journal of Tianjin University (Science and Technology)., 54(02), 161-170, DOI:10.11784/tdxbz202001025, 2021.

Li, Q. and Farmer, D. M.: The generation and evolution of nonlinear internal waves in the deep basin of the South China Sea, Journal of Physical Oceanography., 41(7), 1345-1363, doi:10.1175/2011JPO4587.1, 2011.

Li, Z., You, Y. U., Zhe, S., Zang, J. M., LI, Z. H., Yu, Z. B.: CFD Simulation of Internal Solitary Wave Using the Volume-of-fluid Method within OpenFOAM, DEStech Transactions on Computer Science and Engineering, doi:10.12783/dtcse/mmsta2017/19617, 2017 (mmsta).

Long, R. R.: Some aspects of the flow of stratified fluids: I. A theoretical investigation, Tellus.,5(1), 42-58, doi:10.3402/tellusa.v5i1.8563, 1953.

Lou, S. Y., Tong, B., Hu, H. C., Tang, X. Y.: Coupled KdV equations derived from two-layer fluids, Journal of Physics A: Mathematical and General., 39, 513, doi:10.1088/0305-4470/39/3/005, 2005.

Meng, Q. and Zhang, C.: A third-order KdV solution for internal solitary waves and its application in the numerical wave tank, Journal of Ocean Engineering and Science., 1(2), 93-108, doi:10.1016/j.joes.2016.03.002, 2016.

Menter, F. R., Kuntz, M., and Langtry, R.: Ten years of industrial experience with the SST turbulence model,Turbulence, heat and mass transfer., 4(1), 625-632, 2003.

Michallet, H. and Ivey, G. N.: Experiments on mixing due to internal solitary waves breaking on uniform slopes, Journal of Geophysical Research: Oceans., 104, 13467-13477, doi:10.1029/1999JC900037, 1999.

Miyata, M.: An internal solitary wave of large amplitude, La Mer. 23, 43-48, 1985.

Miyata, M.: Long Internal Waves of Large Amplitude. Springer, Berlin, pp. 399-406. doi:10.1007/978-3-642-83331-1_44. 1988.

OpenFOAM User Guide 2019 http://www.openfoam:docs/.

OpenFOAM User Guide 2019 http://www.openfoam.com/documentation/user-guide.

Osborne, A. R. and Burch, T. L.: Internal solitons in the Andaman Sea, Science., 208, 451-460, doi:10.1126/science.208.4443.451, 1980.

Rayson, M. D., Ivey, G. N., Jones, N. L., Fringer, O. B.: Resolving high-frequency internal waves generated at an isolated coral atoll using an unstructured grid ocean model, Ocean Modelling., 122, 67-84, doi:10.1016/j.ocemod.2017.12.007, 2018.

Sandstrom, H. and Elliott, J. A.: Internal tide and solitons on the Scotian Shelf: A nutrient pump at work, Journal of Geophysical Research: Oceans., 89, 6415-6426, doi:10.1029/JC089iC04p06415, 1984.

Seadawy, A. R.: Exact solutions of a two-dimensional nonlinear Schrödinger equation, Applied Mathematics Letters., 25, 687-691, doi:10.1016/j.aml.2011.09.030, 2012.

Seadawy, A. R., Lu, D., and Yue, C.: Travelling wave solutions of the generalized nonlinear fifth-order KdV water wave equations and its stability, Journal of Taibah University for Science., 11, 623-633,

doi:10.1016/j.jtusci.2016.06.002, 2017.

Shaw, P. T., Ko, D. S., and Chao, S. Y.: Internal solitary waves induced by flow over a ridge: With applications to the northern South China Sea, Journal of Geophysical Research: Oceans., 114(C2), doi:10.1029/2008JC005007, 2009.

Simmons, H. L., Hallberg, R. W., and Arbic, B. K.: Internal wave generation in a global baroclinic tide model, Deep Sea Research Part II: Topical Studies in Oceanography., 51(25-26), 3043-3068, doi:10.1016/j.dsr2.2004.09.015, 2004.

Smedstad, O. M., Hurlburt, H. E., Metzger, E. J., Rhodes, R. C., Shriver, J. F., Wallcraft, A. J., Kara, A. B.: An operational eddy resolving 1/16 global ocean nowcast/forecast system,Journal of Marine Systems.,40, 341-361, doi:10.1016/S0924-7963(03)00024-1, 2003.

Subich, C. J., Lamb, K. G., and Stastna, M.: Simulation of the Navier–Stokes equations in three dimensions with a spectral collocation method, International Journal for Numerical Methods in Fluids., 73(2), 103-129, doi:10.1002/fld.3788, 2013.

Thiem, Ø., Carr, M., Berntsen, J., Davies, P. A.: Numerical simulation of internal solitary wave-induced reverse flow and associated vortices in a shallow, two-layer fluid benthic boundary layer. Ocean dynamics., 61, 857, doi:10.1007/s10236-011-0396-5, 2011.

Turkington, B., Eydeland, A., and Wang, S.: A computational method for solitary internal waves in a continuously stratified fluid, Studies in Applied Mathematics., 85, 93-127, doi:10.1002/sapm199185293, 1991.

Vlasenko, V., Stashchuk, N., and Hutter, K.: Baroclinic Tides: Theoretical Modeling andObservational Evidence, Cambridge University Press., doi:10.5670/oceanog.2006.107, 2005.

Vlasenko, V., Stashchuk, N., Guo, C., Chen, X.: Multimodal structure of baroclinic tides in the South China Sea, Nonlinear Processes in Geophysics., 17(5), 529-543, doi:10.5194/npg-17-529-2010, 2010.

Wang, X., Zhou, J. F., Wang, Z., You, Y. X.: A numerical and experimental study of internal solitary wave loads on semi-submersible platforms, Ocean Engineering., 150, 298-308, doi:10.1016/j.oceaneng.2017.12.042, 2018.

Wilcox, D. C.: Comparison of two-equation turbulence models for boundary layers with pressure gradient, AIAA journal., 31(8), 1414-1421, doi:10.2514/3.11790, 1993.

Xu, C. and Stastna, M.: Instability and cross-boundary-layer transport by shoaling internal waves over realistic slopes, Journal of Fluid Mechanics., 895, doi:10.1017/jfm.2020.389, 2020.

Yuan, G. and Xiao-Yan, T.: A coupled variable coefficient modified KdV equation arising from a two-layer fluid system, Communications in Theoretical Physics., 48, 961-970, doi:10.1088/0253-6102/48/6/001, 2007.

Zhang, Z., Fringer, O. B., and Ramp, S. R.: Three-dimensional, nonhydrostatic numerical simulation of nonlinear internal wave generation and propagation in the South China Sea, Journal of Geophysical Research: Oceans., 116(C5), doi:10.1029/2010JC006424, 2011.

Zhang. H. G., Gu J. B., Jia, H. Q., Gu, B.: A numerical model for internal wave propagation in

continuously stratified ocean, Chinese Journal of Theoretical and Applied Mechanics., 44, 896-903, doi:10.6052/0459-1879-12-195, 2012.